1 **Engineering a molecular electrocatalytic system for energy-efficient ammonia production**

2 **from wastewater nitrate**

3

4 Dean M. Miller[1], Matthew J. Liu[1], Kristen Abels[1], Anna Kogler[2], Kindle S. Williams,[1] William A.

5 Tarpeh[1,2,3*]

6 [1]Department of Chemical Engineering, Stanford University, Stanford, CA, 94305, United States

7 [2]Department of Civil and Environmental Engineering, Stanford University, Stanford, CA, 94305, United

8 States

9 [3]Woods Institute for the Environment, Stanford University, Stanford, California 94305, United States

10

11 *Corresponding author, Email: wtarpeh@stanford.edu. Address: 443 Via Ortega, Room 387, Stanford

12 CA, 94305, United States. Telephone: (650) 497-1324

13

14 Word counts:

15 Abstract: 157 words.

16 Introduction, Results, and Conclusions: 4998 words.

17 Methods: 1640 words.

18 Figures: 6.

19 Tables: 1.

20 Extended Data Figures: 2.

21 Extended Data Tables: 4.

22

23

24

1

Abstract

Haber-Bosch ammonia production has sustained exponential population growth but exacerbated wastewater nitrate pollution. Abundant nitrate pollutants could be refined to purified nitrogenous chemicals with the electrochemical nitrate reduction reaction (NO_3RR). However, the dilute and impure composition of nitrate-bearing wastewaters presents barriers to realizing practical electrocatalytic systems. We address these barriers in our investigation of the model ammonia-selective homogeneous molecular NO_3RR catalyst Co(DIM) in real wastewater and reactive separations architectures. In this work, we elucidate catalysis inhibition mechanisms imposed by magnesium in real wastewaters that decrease nitrate conversion activity by 62.0%. These mechanisms informed our design of electrocatalyst-in-a-box (ECaB): a novel NO_3RR reactive separation that exhibits the lowest reported energy consumption for purified ammonia production (90.0 ± 2.7 kWh kg-N^{-1}). Engineering ECaB's subunit processes enhanced the rate of ammonia production by 20.4×. This work demonstrates a use-informed engineering approach that iterates between mechanistic insights and unit process-level performance of electrochemical wastewater refining systems in complex aqueous streams.

1. Introduction

Circular wastewater refining processes can responsibly manage waste streams and sustainably produce chemical commodities, including nitrogen compounds. Conventionally, nitrogenous commodity products are derived from ammonia-nitrogen made by the Haber-Bosch (HB) process. HB is highly energy-efficient but contributes 1-2% of global carbon dioxide emissions.[1] The majority of HB-nitrogen is used as fertilizer,[2] but highly distributed cropland does not match the scale of the fewer than 100 HB centralized facilities globally.[3] As a result, transport costs can comprise more than half the price of fertilizers, which motivates distributed ammonia production.[3] Meanwhile, 24-54% of HB-nitrogen is discharged from anthropogenic processes as aqueous nitrate (NO_3^-) and ammonium (NH_4^+).[4] Refining these fugitive nitrogen emissions into a tunable, diverse portfolio of products could generate 19 billion USD annually.[4] The electrocatalytic NO_3^- reduction reaction (NO_3RR) to ammonia can refine nitrate-rich wastewaters that contain 19-48 Tg NO_3^--N globally per year.[4] Electrified NO_3RR processes will readily integrate with renewable and decentralized energy sources, which could enable ammonia production at sites of wastewater generation. This circular NO_3^- refining paradigm can improve sanitation access, expand nitrogen commodity access, and offset costs and emissions of industrial ammonia production.

Despite the large overall flux of anthropogenic nitrogen discharges to the environment, most NO_3^- is contributed by dilute and impure wastewater sources.[5] Both point sources (e.g., municipal wastewater) and nonpoint sources (e.g., agricultural runoff) generally contain less than 50 mg NO_3^--N L^{-1} (3.6 mM).[6–11] Municipal and agricultural wastewaters are also impure; they contain co-constituents (e.g., organic/inorganic ions, organic carbon, suspended solids) that compete for catalyst active sites, degrade catalysts over time, passivate electrode surfaces, and alter solution pH outside of catalyst operating ranges.[12–14] In contrast to real wastewaters, NO_3RR electrocatalysts are most heavily documented with NO_3^- concentrations above 100 mM (i.e., concentrated) in synthetic (i.e., pure) electrolytes.[15–25] NO_3^- refining research must overcome the difference in NO_3^- concentration and purity between catalysis investigations and real wastewaters to be relevant for wastewater treatment and chemical manufacturing.

3

65 Homogeneous molecular catalysts are promising for wastewater NO_3^- refining because their

66 atomically precise reactivity could overcome both dilute and impure wastewater conditions;[26] however,

67 these catalysts are rarely explored for wastewater treatment because they require separation. The ligand

68 structures of molecular catalysts promote high reactant and product selectivities that could enhance NO_3RR

69 faradaic efficiency (FE) and reaction rates to total ammonia nitrogen (TAN; the sum of NH_4^+-$N_{(aq)}$ and NH_3-

70 $N_{(aq)}$) in dilute NO_3^- solutions. The metal complex 2,3-dimethyl-1,4,8,11-tetraazacyclotetradeca-1,3-diene

71 (DIM) with a Co metal center, abbreviated Co(DIM), yields TAN as its major product and suppresses the

72 competitive hydrogen evolution reaction (HER) in aqueous conditions from pH 3.5 to 10.1.[27] Co(DIM) is

73 easily synthesized[28] and exemplifies untapped benefits to employing molecular electrocatalysts for

74 wastewater refining. The positively-charged metal center of Co(DIM) facilitates binding of negatively-

75 charged NO_3^-.[27] Additionally, homogeneous electrocatalytic processes directly scale with volume[29] (e.g.,

76 Fenton catalysts,[30] porphyrins for PFAS remediation[31]) and can use economical carbonaceous electrode

77 materials. Rational design principles for molecular electrocatalyst design, operation, and separation in

78 wastewater refining processes are currently ill-defined because few use-informed investigations of

79 homogeneous catalysis in real wastewaters exist.

80 Likewise, rational design of wastewater refining unit processes is hampered by a dearth of

81 electrochemical investigations that integrate reactions and separations, or reactive separations.[4,32]

82 Consequently, unit process performance (namely efficiencies, rates, and energy consumption) is difficult

83 to benchmark against incumbent wastewater management processes. Reactive separations can overcome

84 the challenges of dilute and impure wastewaters to enable NO_3^- extraction, NO_3^- conversion to TAN, and

85 purified TAN recovery.[4,33] However, few investigations of reactive separations in real wastewater exist,[34–

86 36] and even fewer exist for dilute wastewaters.[37] Our recent work demonstrated that homogeneous

87 electrocatalysis in existing NO_3RR reactive separation architectures can produce purified TAN

88 $((NH_4)_2SO_{4(aq)})$.[38] Elevating this preliminary demonstration to rationally designed unit processes requires

89 investigation of interfacial phenomena imposed by catalytically influential wastewater species.[14,33]

4

90   To address the rational design challenges imposed by dilute and impure NO_3^-, we sought to

91   explicitly investigate interfacial mechanisms that govern Co(DIM)-mediated NO_3RR reactive separations

92   performance in real wastewaters, and to leverage these insights toward engineering novel high-performing

93   molecular catalysis systems. By investigating catalysis (via electrolysis, amperometry, and spectroscopy)

94   in a systematic suite of simulated and real wastewater electrolytes, we elucidated the mechanistic influences

95   of inorganic ions on reactor performance. More specifically, we investigated the role of bulk and interfacial

96   ionic composition on activity and FE, and found that magnesium ions play a deterministic role in electrode

97   fouling. These mechanistic insights enabled rational design of a novel reactive separations architecture,

98   electrocatalyst-in-a-box (ECaB). Our first ECaB iteration (proof-of-concept ECaB) exhibited sustained

99   activity, high FE, and low energy consumption for several cycles to treat a real, NO_3^--bearing wastewater:

100   municipal secondary effluent. Proof-of-concept ECaB enabled long-term evaluation and benchmarking of

101   the full unit process and its subunit processes against related NO_3RR efforts and conventional nitrogen

102   management (wastewater treatment and HB-ammonia production). Proof-of-concept ECaB also generated

103   a high-purity TAN product with the lowest reported energy consumption (90.0 ± 2.7 kWh kg-N^{-1}) for any

104   NO_3RR reactive separation process to date. In a second, improved iteration (subunit engineered ECaB), we

105   leveraged reactor design to improve subunit process rates toward scalable performance targets. Ultimately,

106   our novel findings span from the microenvironment to the unit process scale and contribute to the informed

107   design of catalysts, electrode and membrane interfaces, and electrochemical reactors. This study

108   demonstrates a use-informed, iterative approach to wastewater electrocatalysis that guides the development

109   of efficient and practical reactors for circular chemical manufacturing.

110

2. Results

Because the primary NO_3^--rich wastewaters are municipal secondary effluent and fertilizer runoff, NO_3RR processes must operate with feed compositions of dilute NO_3^- (<4 mM), low conductivity (<2 mS cm^{-1}), and water hardness (i.e., presence of divalent metal cations).[37,38] We collected and conducted experiments in a representative secondary effluent (Table S1) containing 120 mg NO_3^-/L (28 mg NO_3^--N/L, 2.0 mM NO_3^-) and a matrix of anions, alkaline earth metal cations, suspended solids, and organic and inorganic carbon. Within this complex composition, we sought to uncover the promoting or inhibiting effects of specific wastewater constituents on Co(DIM)-mediated NO_3RR (Section 2.1). Toward this goal, we assessed NO_3RR performance as a function of electrolyte composition (Section 2.1.1) and described generalizable interfacial mechanisms that influence Co(DIM)-mediated NO_3RR behavior (Section 2.1.2). These insights informed the design and development of the novel reactive separations process ECaB (Section 2.2). Proof-of-concept ECaB (Section 3.2.1) demonstrated robust performance with real wastewater and enabled systematic comparisons to previous NO_3RR investigations (Section 3.2.2). Finally, subunit engineered ECaB demonstrated improved subunit process rates toward tractable performance targets (Section 3.2.3).

6

126 **_2.1: Effects of electrolyte composition on Co(DIM)-mediated NO$_3$RR_**

127 _2.1.1: Effects of bulk electrolyte composition on observed NO$_3$RR performance_

128
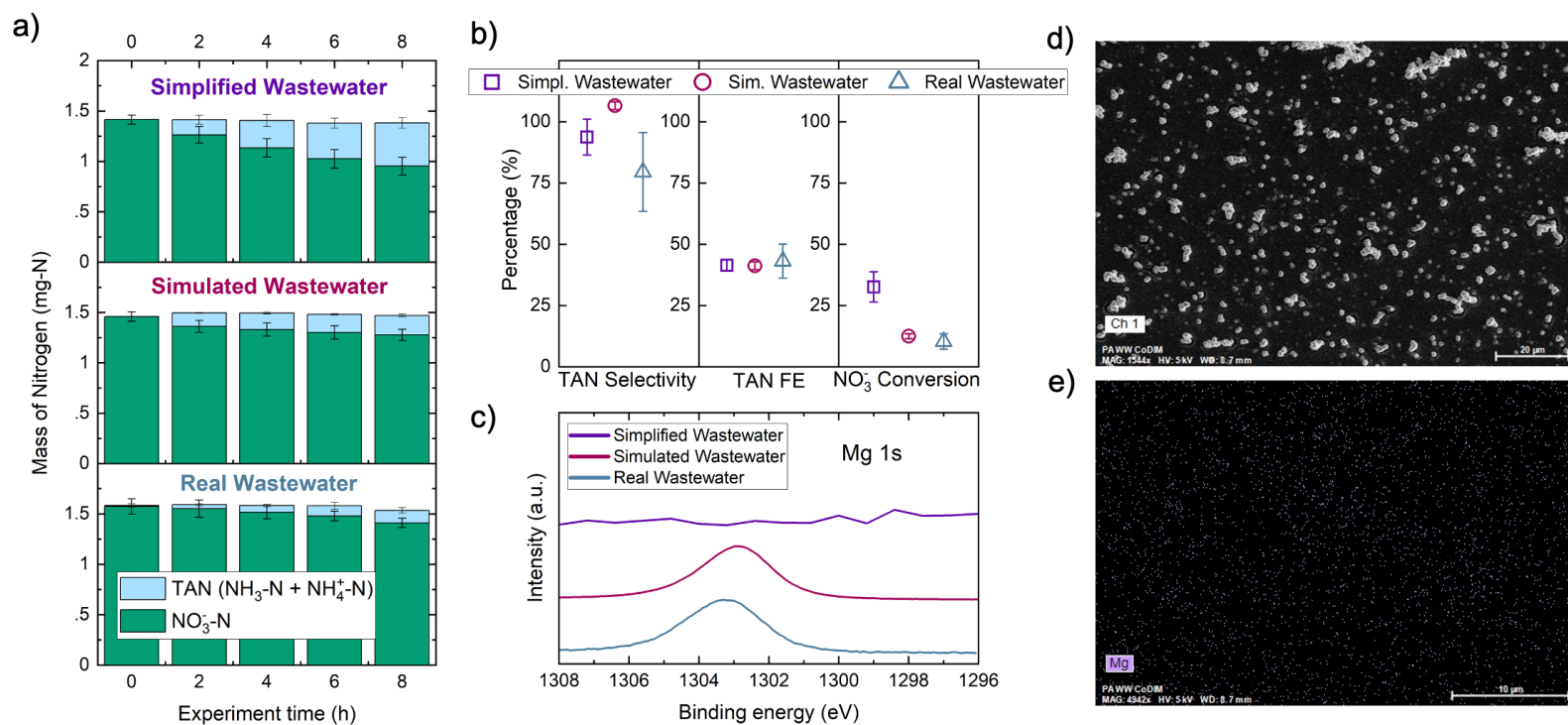
129

130 **Fig. 1.** a) Mass balance of aqueous nitrogen species as a function of time during two-chamber controlled-potential electrolysis (CPE) experiments

131 at –1.05 V vs. Ag/AgCl performed in three electrolytes: 8 mM Co(DIM) in simplified wastewater, 8 mM Co(DIM) in simulated wastewater, and 8

132 mM Co(DIM) in real wastewater. Error bars represent ± one standard deviation from triplicate experiments (n=3). For all three electrolytes, NO$_3^-$-

133 N and TAN closed the nitrogen mass balance within ± 3%. No TAN was detected after CPE without NO$_3^-$ (Fig. S6), confirming that measured TAN

7

134   was the result of NO$_3$RR. The closed mass balance and catalytic TAN formation support that NO$_3$RR selectivity to TAN remained near 100% in all

135   three electrolytes tested, consistent with previous investigations.[27,38] b) Cumulative TAN selectivity, TAN faradaic efficiency, and NO$_3^-$ conversion

136   for 8-hour CPE experiments. c) Mg 1s XPS spectra of the glassy carbon plate cathode after CPE experiments. After CPE the electrode was rinsed

137   with nanopure water and blown dry with N$_2$ before XPS and SEM-EDS analysis. d) SEM image and e) Mg EDS map of glassy carbon plate cathode

138   after a CPE experiment in real wastewater, showing dispersed deposits of Mg on the surface.

139   Cyclic voltammetry (CV) and controlled-potential electrolysis (CPE) elucidated Co(DIM)-

140 mediated NO_3RR catalytic activity and selectivity as a function of electrolyte composition. Prior work

141 showed that the rate of homogeneous Co(DIM)-mediated NO_3RR is independent of pH and is first order

142 with respect to [Co(DIM)] (0.5-5 mM) and $[NO_3^-]$ (5-100 mM).[27] Extended Data Fig. 2 shows that

143 homogeneous NO_3RR catalysis is first order with respect to [Co(DIM)] even at low excess factors ($[NO_3^-]$

144 divided by [Co(DIM)]) than tested previously (i.e., < 2), indicating catalysis outpaces bulk-phase catalyst

145 diffusion. Additionally, the catalytic waveforms of 8 mM Co(DIM) are effectively identical in synthetic

146 electrolyte (6.2 mM NaCl + 2 mM $NaNO_3$) and in the real wastewater (Fig. S5) at 100 mV s^{-1}, implying

147 intrinsic catalytic activity is unaffected by complex wastewater electrolyte. This conclusion was tested in

148 two-chamber CPE experiments (Fig. 1a) with three catholytes (Table S1). TAN selectivity (93.8 ± 7.3%

149 for simplified, 106.5 ± 1.6% for simulated, and 79.5 ± 16.1% for real wastewater) and FE (41.4 ± 2.4% for

150 simplified, 41.2 ± 1.6% for simulated, and 43.1 ± 7.0% for real wastewater) remained relatively unaffected

151 by electrolyte composition; neither the difference between simplified and simulated CPEs ($p = 0.13 > 0.05$

152 for selectivity, $p = 0.17 > 0.05$ for FE) nor the difference between simplified and real CPEs ($p = 0.14 > 0.05$

153 for selectivity, $p = 0.62 > 0.05$ for FE) were statistically significant (Fig. 1b). Co(DIM) therefore enabled

154 selective NO_3RR to TAN in all dilute NO_3^- conditions. However, NO_3^- conversion was significantly lower

155 in simulated (12.4 ± 1.0%, $p = 0.029 < 0.05$) and real (10.3 ± 3.1%, $p = 0.0083 < 0.05$) wastewaters compared

156 to simplified wastewater (32.6 ± 6.1%). Simulated wastewater was also a high-fidelity proxy of real

157 wastewater, as demonstrated by the lack of significant difference in conversion between these two streams

158 ($p = 0.31 > 0.05$). Therefore, inorganic ionic constituents in the wastewater matrix were most responsible

159 for inhibiting catalyst activity.

160   Whereas NO_3RR activity was strongly influenced by wastewater impurities, the relatively low

161 FE_{TAN} was primarily influenced by NO_3^- concentration. Under purely kinetic conditions,[39] Co(DIM)-

162 mediated NO_3RR is first order in [Co(DIM)] and $[NO_3^-]$, motivating the high catalyst concentrations

163 employed in CVs and CPEs. However, purely kinetic conditions do not apply in our CPE experiments

9

164   because the low excess factor imposed by the wastewater caused substrate consumption in the RDL, and

165   consequently a significant amount of current was consumed by non-catalytic reductions of Co(DIM).

166   Several control CPE experiments were performed to quantify non-catalytic charge allocation (i.e., FE). CPE

167   at $-0.75V_{Ag/AgCl}$ (-0.99 V vs. first reduction, $+0.25$ V vs. second reduction) in simplified wastewater (6.2

168   mM NaCl + 2 mM NaNO$_3$) served as a proxy for non-catalytic charge toward the first reduction of Co(DIM);

169   CPE at $-1.05V_{Ag/AgCl}$ in a modified simplified wastewater (6.2 mM NaCl + 0 mM NaNO$_3$) served as a

170   proxy for non-catalytic charge toward the first and second reductions. The sum of charge associated with

171   non-catalytic reductions of Co(DIM) accounts for 89.4% of charge passed in the simplified wastewater

172   CPEs (Fig. S6, Fig.S7), reasonably closing the balance of FE. Notably, the non-catalytic charge passed

173   (49.3% FE) exceeded the catalytic charge passed (41.4 ± 2.4% FE). The excess factor therefore significantly

174   influences the ratio of activated Co(DIM) molecules that successfully perform NO$_3$RR in the homogeneous

175   phase.

176   Because only NO$_3^-$ conversion was significantly changed as a function of electrolyte composition,

177   we hypothesized that electrode fouling in simulated and real wastewater reduced the observed NO$_3$RR rate

178   by impeding Co(DIM) activation at the heterogeneous electrode-electrolyte interface. Visible deposits were

179   present on the electrode after 8 hours for all three electrolytes (Fig. S8), prompting spectroscopic and

180   electrochemical characterization of the GC surface. Based on simulated wastewater exhibiting electrode

181   fouling, we expected that hardness (e.g., Mg^{2+}, Ca^{2+}) and HCO$_3^-$/CO$_3^{2-}$ ions were precipitate components.

182   XPS (Fig. 2c) and SEM/EDS (Fig. 2d-e) revealed magnesium on the GC surface for real and simulated

183   wastewater. The pH required for precipitation of Mg(OH)$_2$ from 1.5 mM Mg^{2+} is 9.8 (Table S2). Because

184   the bulk pH of all three catholytes remained below 9.8 (Fig. S9), the interfacial pH in the RDL likely

185   exceeded pH 9.8, which is common under reducing electrochemical conditions.[40] No significant

186   precipitation of Ca^{2+} was observed by EDS after real wastewater CPE (Fig. S10, Fig. S11), implying that

187   the interfacial pH remained below the 12.8 required to precipitate Ca(OH)$_2$ from 1.9 mM Ca^{2+}. We also

188   compared the catalytic activity and charge transfer resistance of the deposits formed on GC cathodes in

189 simplified and real wastewaters. In rinse tests, both deposits were less active than homogeneous Co(DIM)

190 and were not selective for TAN or NO_2^- (Fig. S12, Fig. S13). Thus, we did not consider the deposits catalytic.

191 The charge transfer resistance between the electrode surface and homogeneous Co(DIM) at the open circuit

192 potential (OCP) was greater for the real deposit (R_{ct} = 310 kΩ) than for the simplified deposit (R_{ct} = 189.4

193 kΩ) and the pristine GC surface (R_{ct} = 132.7 kΩ) (Fig. S14). In conjunction with the insensitivity of TAN

194 FE and selectivity to electrolyte composition (Fig. 2b), greater charge transfer resistance suggested that

195 catalysis was heterogeneously inhibited by Mg deposition and that the homogeneous Co(DIM)-mediated

196 NO_3RR mechanism was unaffected by real wastewater impurities.

2.1.2: Interfacial mechanism of catalysis inhibition by Mg^{2+}
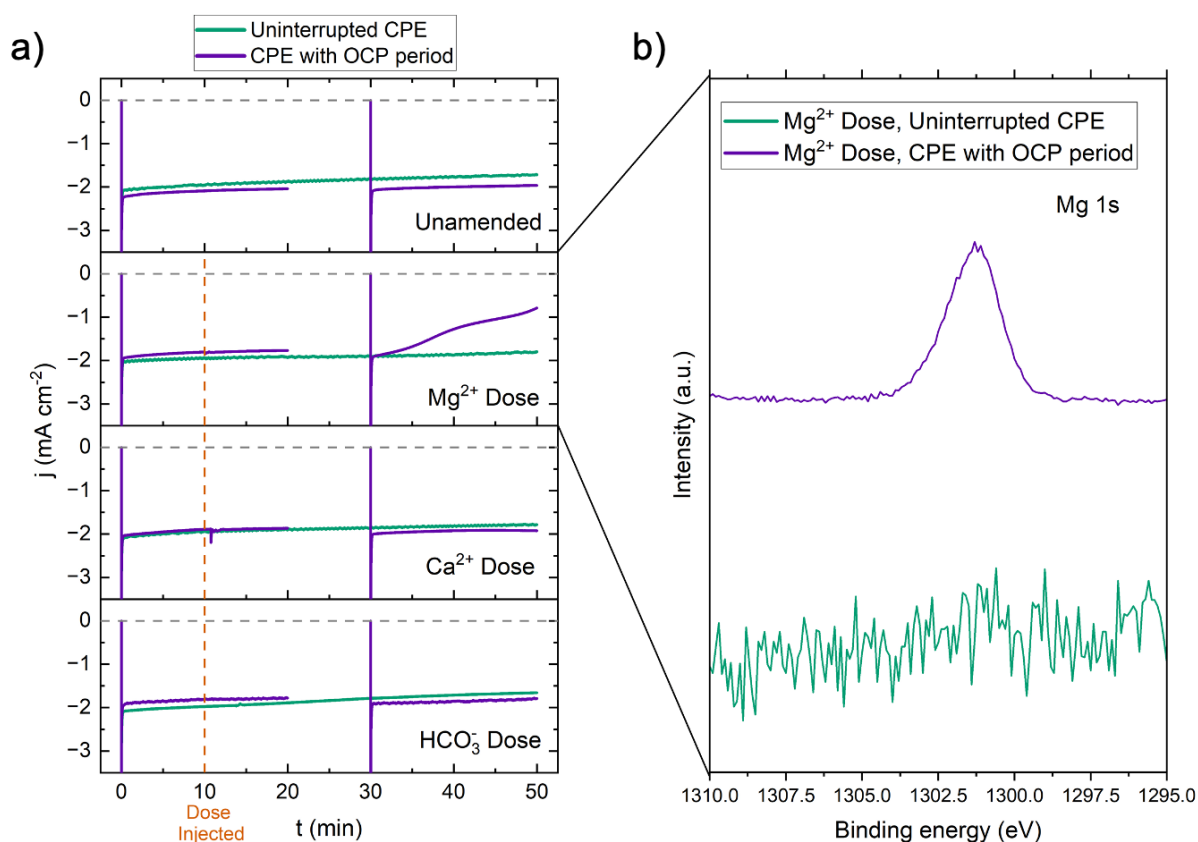
Fig. 2. (a) Current density vs. time of RDE CPEs -1.05 $V_{Ag/AgCl}$ with suspected foulants manually dosed

into the electrolyte at $t = 10$ min (no contaminant dose, 28 μL 1 M $MgCl_2$, 30 μL 1 M $NaHCO_3$, 38 μL 1 M

$CaCl_2$). Two experiment conditions were compared: the first experiment held -1.05 $V_{Ag/AgCl}$ for the full 50

minutes (green trace), and the second experiment introduced a period of open circuit potential (OCP) from

$t = 20$ min to $t = 30$ min. The counter electrode was a 6.4 mm graphite rod and the reference electrode was

a Ag/AgCl (4.0 M KCl) electrode. The RDE was operated at 25 rotations per minute (RPM) because both

catalytic current (for simplified wastewater) and inhibition (for real wastewater) were observed at this

rotation rate (SI Section S4.1, Fig. S15). (b) Mg 1s XPS of the glassy carbon RDE electrode post Mg^{2+}

dose CPE for both the uninterrupted CPE and the CPE with OCP period.

209   To identify specific inhibiting species, we dosed a small volume (28-38 µL, matching real

210   wastewater concentrations, Table S1) of 1 M solutions ($MgCl_2$, $CaCl_2$, and $NaHCO_3$) into simplified

211   wastewater electrolyte with 8 mM Co(DIM) (Fig. 2a). Current density remained unchanged for all dosed

212   species during uninterrupted RDE CPE experiments (green trace), contrary to the RDE CPE in real

213   wastewater showing a distinct decay in current density (Fig. S15). However, introducing an open circuit

214   potential (OCP; purple trace) period caused a decay in current density for the Mg^{2+} dose experiment, but

215   not for Ca^{2+} or HCO_3^-. XPS detected Mg deposits on the GC surface with an OCP period but not for

216   uninterrupted CPE (Fig. 2b), further highlighting Mg^{2+} as the major foulant responsible for catalysis

217   inhibition. If Mg^{2+} is homogeneously dispersed throughout the electrolyte when CPE begins (the case for

218   CPE after an OCP period), Mg^{2+} can specifically adsorb to the GC cathode. When the pH conditions for

219   precipitation are met in the RDL, adsorbed Mg^{2+} ions form Mg deposits (most likely $Mg(OH)_2$ based on

220   the solubility product quotient, Q_{sp}, versus the solubility product consant, K_{sp}; Table S2), passivating the

221   electrode. Conversely, if the RDL is established prior to introducing Mg^{2+} (the case for uninterrupted CPEs),

222   positively-charged Co(DIM) in the RDL electrostatically and/or sterically impedes specific adsorption of

223   Mg^{2+}. Thus, even if the pH conditions for precipitation are met in the RDL, repulsive interactions between

224   Co(DIM) and Mg^{2+} may preclude precipitation and passivation for minutes to hours. To further confirm the

225   role of Mg^{2+}, we demonstrated prolonged passivation in two ways. First, a longer CPE following Mg^{2+} in

226   RDE (Fig. S16) showed no change in current density over 40 min but showed an immediate decay in current

227   density after an OCP period. Second, two-chamber CPEs for 8 hours (same two-chamber CPE setup as in

228   Fig. 1; closed nitrogen mass balances in Fig. S17-S20) with contaminant doses showed <6.3% change in

229   NO_3^- conversion and TAN production (Fig. S21). Thus activity, selectivity, and FE are unaffected by Mg^{2+},

230   Ca^{2+}, and HCO_3^- doses when Co(DIM) protects against passivation.

231   Magnesium precipitation during Co(DIM)-mediated electrocatalytic NO_3RR is generalizable to

232   reductive homogeneous electrocatalysis and to NO_3RR (heterogeneous or homogeneous) in real

233   wastewaters. Similar precipitation processes have been observed in homogeneous CO_2 reduction

234   electrocatalysis,[41] and water hardness (i.e., Mg^{2+}, Ca^{2+}) has been shown to decrease heterogeneous NO_3^-

13

235 removal.[14] In the secondary effluent used in this work (1.5 mM Mg^{2+}), a negligible proportion of Mg^{2+}

236 present was consumed to form a passivating cathode deposit (Fig. S22). Other nitrate-rich wastewaters like

237 polluted groundwaters, reverse osmosis brines, and ion exchange brines may contain higher Mg^{2+}

238 concentrations (up to 84 mM),[42] increasing the likelihood of forming precipitates. Mg^{2+} electrode fouling

239 is likely a widespread barrier to implementation. A reactive separation system could conceivably perform

240 uninhibited NO_3RR directly in the native wastewater if divalent cations are repelled by near-surface

241 confined Co(DIM) molecules. This insight motivates repulsive moieties at the electrode-electrolyte

242 interface as a design principle for the microenvironment of homogeneous and heterogeneous catalyst

243 systems. Electrode and catalyst design (e.g., heterogeneous molecular catalysts, single-atom catalysts,

244 ionomer coatings) could protect the cathode from passivation, but would not address the low TAN FE

245 induced by inherently low NO_3^- concentrations in real wastewaters. The remainder of this study addresses

246 cathode protection and FE_{TAN} with reactive separations that selectively extract and up-concentrate NO_3^-

247 (and reject Mg^{2+}) from wastewater before catalysis.

2.2: Electrocatalyst-in-a-box (ECaB)

249   We mitigated cathode passivation in NO_3RR by pre-catalysis extraction of NO_3^- from wastewater

250 via reactive separations. Extracting NO_3^- into a synthetic electrolyte for Co(DIM)-mediated NO_3RR could

251 be achieved by electrochemical separations such as electrodialysis,[43] capacitive deionization,[44] or

252 electrosorption,[37] but in low-conductivity NO_3^--rich wastewaters, electrochemical extraction can dominate

253 the total process energy consumption.[33,37] This observation motivates low-energy extraction methods like

254 Donnan membrane dialysis.[45] Because Donnan equilibrium conditions are governed by electrochemical

255 potentials (not concentrations) across the membrane, NO_3^- ions can diffuse against their concentration

256 gradient by exchanging with high-activity receiver solution anions (e.g., Cl^-). If the receiver solution

257 volume is less than the feed solution (wastewater) volume, NO_3^- in the receiver solution can be substantially

258 up-concentrated relative to the feed concentration. The resulting receiver solution is an ideal electrolyte for

259 NO_3RR because of its high conductivity, high NO_3^- concentration, and absence of Mg^{2+}. Donnan dialysis

14

260   (DD) can also obviate challenges imposed by complex electrolyte compositions (e.g., high [Cl⁻], divalent

261   ions, organics), like unselective ion extraction, high energy consumption, and high capital costs.[45] In this

262   section, we report a combined DD, NO$_3$RR, and ammonia stripping system coined electrocatalyst-in-a-box

263   (ECaB; Fig. 3a).

264

2.2.1: Proof-of-concept ECaB with real wastewater
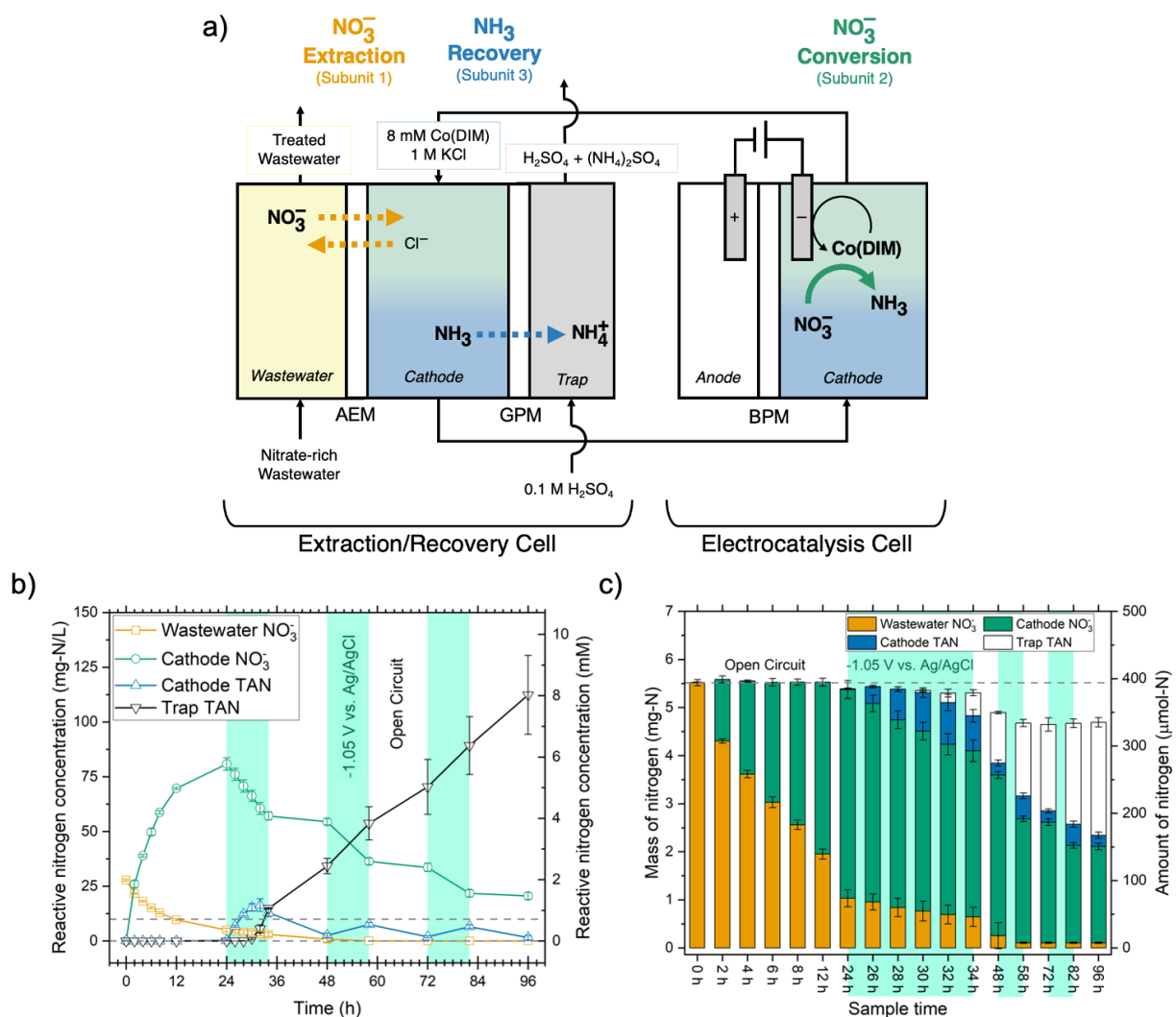
Fig. 3. (a) Electrocatalyst-in-a-box (ECaB) schematic. Wastewater-NO_3^- extraction (subunit process 1,

orange) is achieved by Donnan dialysis (DD) in the extraction/recovery cell (left) where NO_3^- ions exchange

with Cl^- ions due to an electrochemical potential gradient across the anion exchange membrane (AEM).

The catholyte recirculates between the extraction/recovery cell and the bipolar membrane (BPM)-separated

electrocatalysis cell (right) where Co(DIM)-mediated NO_3RR (subunit process 2, green) converts NO_3^- to

TAN. As the catholyte basifies under reducing conditions, the majority of TAN exists as NH_3 that is

recovered (subunit process 3, blue) by diffusing across the gas-permeable membrane (GPM) into the acidic

trap chamber. (b) NO_3^- and TAN concentrations and (c) nitrogen mass balance for electrocatalyst-in-a-box

16

275   experiments. Error bars represent ± one standard deviation from triplicate experiments (n=3). Detailed

276   experimental parameters of ECaB tests can be found in Materials & Methods Section 2.2.3. Time periods

277   where the electrochemical cell was held at open circuit (OCP; 0-24 h, 34-48 h, 58-72 h, 82-96 h) are

278   indicated by a white background and time periods where the electrochemical cell was held at -1.05 $V_{Ag/AgCl}$

279   (24-34 h, 48-58 h, 72-82 h) are indicated by a green background. Applied potentials were held for 10 h at

280   a time to keep Co(DIM) in its stable operating pH regime.[27,38] The dashed line in panel (b) indicates the

281   drinking water limit of 10 mg NO_3-N/L.

282

283

https://doi.org/10.26434/chemrxiv-2023-1s6n8-v2 **ORCID:** https://orcid.org/0000-0002-7970-3475 Content not peer-reviewed by ChemRxiv. **License:** CC BY-NC-ND 4.0

284   The ECaB unit process performs three subunit processes—wastewater NO_3^- extraction, NO_3^-

285   conversion to TAN, and TAN recovery—in a configuration of four electrolyte reservoirs (wastewater,

286   catholyte, anolyte, and trap) and two applied potential conditions (OCP and -1.05 $V_{Ag/AgCl}$). First, DD

287   facilitates wastewater NO_3^- extraction via ion exchange with catholyte Cl^- ions across an AEM. To up-

288   concentrate the catholyte NO_3^-, we used four times as much municipal secondary effluent volume (200 mL)

289   as catholyte volume (50 mL). In proof-of-concept ECaB experiments (Fig. 3b), the catholyte NO_3^- was up-

290   concentrated by 2.9 times from 27.8 ± 0.5 mg-N/L (2.0 ± 0.04 mM) to 80.8 ± 2.8 mg-N/L (5.8 ± 0.2 mM)

291   over the first 24 h OCP period when only DD was active. Meanwhile, the wastewater NO_3^- concentration

292   decreased to 5.0 ± 0.9 mg-N/L (0.36 ± 0.06 mM), below the drinking water standard of 10 mg-N/L.[46] DD

293   requires no electrochemical energy input to extract and up-concentrate NO_3^- in the catholyte, only the

294   embedded energy requirement to produce NaCl. DD paired with NO_3RR therefore subverts the energy

295   consumption-reaction rate tradeoff in NO_3RR reactive separations. At 24 h, -1.05 $V_{Ag/AgCl}$ was applied to

296   stimulate Co(DIM)-mediated NO_3RR (24-34 h), corresponding to a decrease in catholyte NO_3^- and an

297   increase in catholyte TAN. -1.05 $V_{Ag/AgCl}$ was held for 10 h periods to keep Co(DIM) in its stable operating

298   pH regime;[27,38] operation for longer than 10 h in these experiments resulted in catholyte pH >11 and

299   significant decrease in FE_{TAN}. After 6 h of CPE, the catholyte pH (Fig. S23) was sufficiently alkaline for

300   catholyte TAN to exist primarily as NH_3 ($pKa_{NH_4^+/NH_3} = 9.25$), which volatilized, crossed the GPM, and

301   was recovered in the acid trap (0.1 M H_2SO_4). ECaB was recirculated overnight (34-48 h) at open circuit

302   as the remaining TAN migrated across the GPM. At 48 h, the catholyte was adjusted back to pH 6 with

303   ~200 µL 10 wt% HCl to keep Co(DIM) in its stable operating pH regime[27,38] before a second cycle of CPE

304   (48-58 h) and OCP (58-72 h) began. ECaB experiments were performed for three cycles for a total of 96 h

305   (30 cumulative hours of CPE) to demonstrate proof-of-concept. The total measured N masses (Fig. 4c) at

306   24 h, 48 h, 72 h, and 96 h accounted for $97.6 \pm 1.4\%$, $88.7 \pm 5.1\%$, $84.1 \pm 2.7\%$, and $84.9 \pm 1.8\%$ of the

307   influent wastewater NO_3^--N. We hypothesize that binding of NH_3 to Co(DIM) was the largest contributor

308   to unclosed mass balances because the largest changes occurred during recirculation at OCP from 34-48 h

18

309   and Co(DIM) in its Co(III) oxidation has a high NH_3 binding capacity (at least 1.6 mM TAN / mM Co(DIM;

310   Fig. S24). Critically, the wastewater remained circumneutral for the duration of experiments (pH 7.07 $\pm$

311   0.25 at t = 96 h, Fig. S23), demonstrating the potential feasibility of downstream treatment for water reuse.

312   The combination of membrane-based DD and ammonia stripping isolates the homogeneous Co(DIM)

313   solution from the wastewater feed and the TAN product (Fig. S25), enabling treated wastewater recovery,

314   product TAN recovery, and homogeneous catalyst reuse. This catalyst reuse is similar to catalyst-in-a-cup[47]

315   (in which thermal homogenous catalysts are separated from solvents, reactants, and products in chemical

316   production), inspiring the ECaB name.

2.2.2: Reactive separations unit and subunit process performance metrics
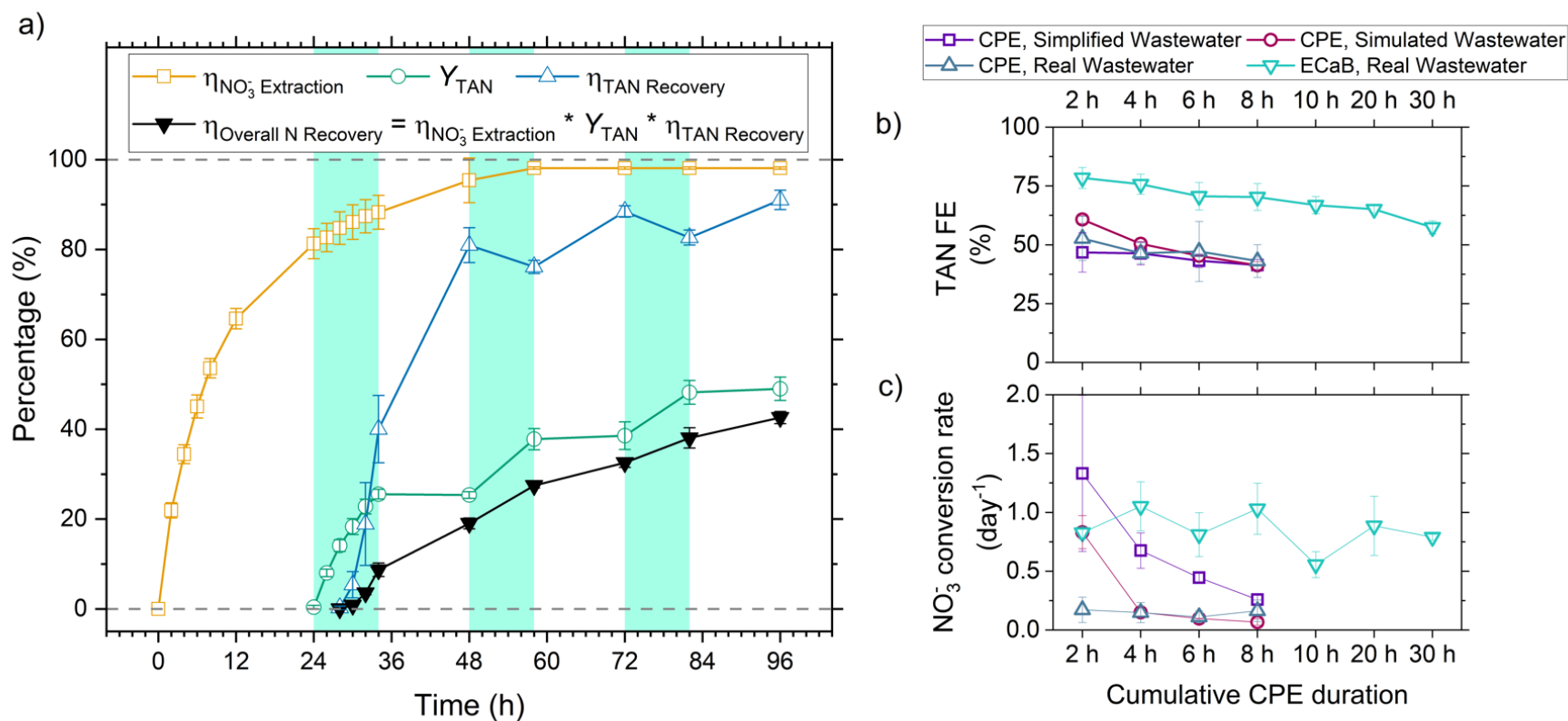
Fig. 4. (a) Cumulative NO_3^- extraction efficiency ($\eta_{NO_3^- \text{ Extraction}}$), TAN yield ($Y_{TAN}$), TAN recovery efficiency ($\eta_{TAN \text{ Recovery}}$), and overall nitrogen

recovery efficiency ($\eta_{Overall N \text{ Recovery}}$) during ECaB experiments. Error bars represent ± one standard deviation from triplicate experiments (n=3).

Detailed experimental parameters of ECaB tests can be found in Materials & Methods Section 2.2.3. Time periods where the electrochemical cell

20

322   was held at open circuit (OCP; 0-24 h, 34-48 h, 58-72 h, 82-96 h) are indicated by a white background and time periods where the electrochemical

323   cell was held at –1.05 $V_{Ag/AgCl}$ (24-34 h, 48-58 h, 72-82 h) are indicated by a green background. (b) Cumulative FE_{TAN} as a function of cumulative

324   CPE duration. (c) Pseudo-instantaneous NO_3^- conversion rate (nitrate converted over one sample period divided by the preceding sample period

325   nitrate concentration; Equation S5.1.16). Equations used to calculate efficiency and rate metrics can be found in SI Section S5.1.

21

326   By decomposing NO_3^- refining performance into subunit processes (NO_3^- extraction, NO_3^-

327   conversion, and TAN recovery), ECaB facilitates systematic comparisons of NO_3^- refining studies in terms

328   of efficiencies, rates, and energy consumption (Extended Data Tables 1-4).[48] The overall nitrogen recovery

329   efficiency $\left(\eta_{\text{Overall N Recovery}} = \frac{\text{mol N}_{\text{recovered}}(t)}{\text{mol N}_{\text{wastewater}}(\text{initial})}\right)$ is the product of NO_3^- extraction efficiency, TAN yield,

330   and TAN recovery efficiency (Section S5.1 and Fig. S26). For ECaB, $98.1 \pm 0.3\%$ of wastewater NO_3^- was

331   extracted by the end of the 96 h experiments, with $81.3 \pm 3.3\%$ extracted in the first 24 hours (Fig. 4a). 60.8

332    $\pm 1.1\%$ of extracted NO_3^- was converted via Co(DIM)-mediated NO_3RR and $91.0 \pm 2.1\%$ of produced TAN

333   was recovered in the trap. Overall, $42.6 \pm 1.4\%$ of influent wastewater NO_3^--N was recovered as TAN.

334   Proof-of-concept ECaB prevented cathode Mg fouling and enabled sustained NO_3^- conversion via selective

335   NO_3^- extraction (Fig. S27-S29). Despite having a more complex composition, ECaB with real wastewater

336   outperformed CPE in simplified wastewater in terms of FE_{TAN} (Fig. 4b) and NO_3^- conversion rate (Fig. 4c).

337   Additionally, Mg^{2+} was not detected in the catholyte nor on the GC surface by XPS (Fig. S30) or EDS (Fig.

338   S31), reinforcing that Co(DIM)-mediated NO_3RR activity in ECaB was not inhibited by cathode

339   passivation. ECaB exemplifies a reactive separation process for treating real wastewater, and outperforms

340   a simplified (i.e., ideal) system driven by insights of wastewater-induced inhibition.
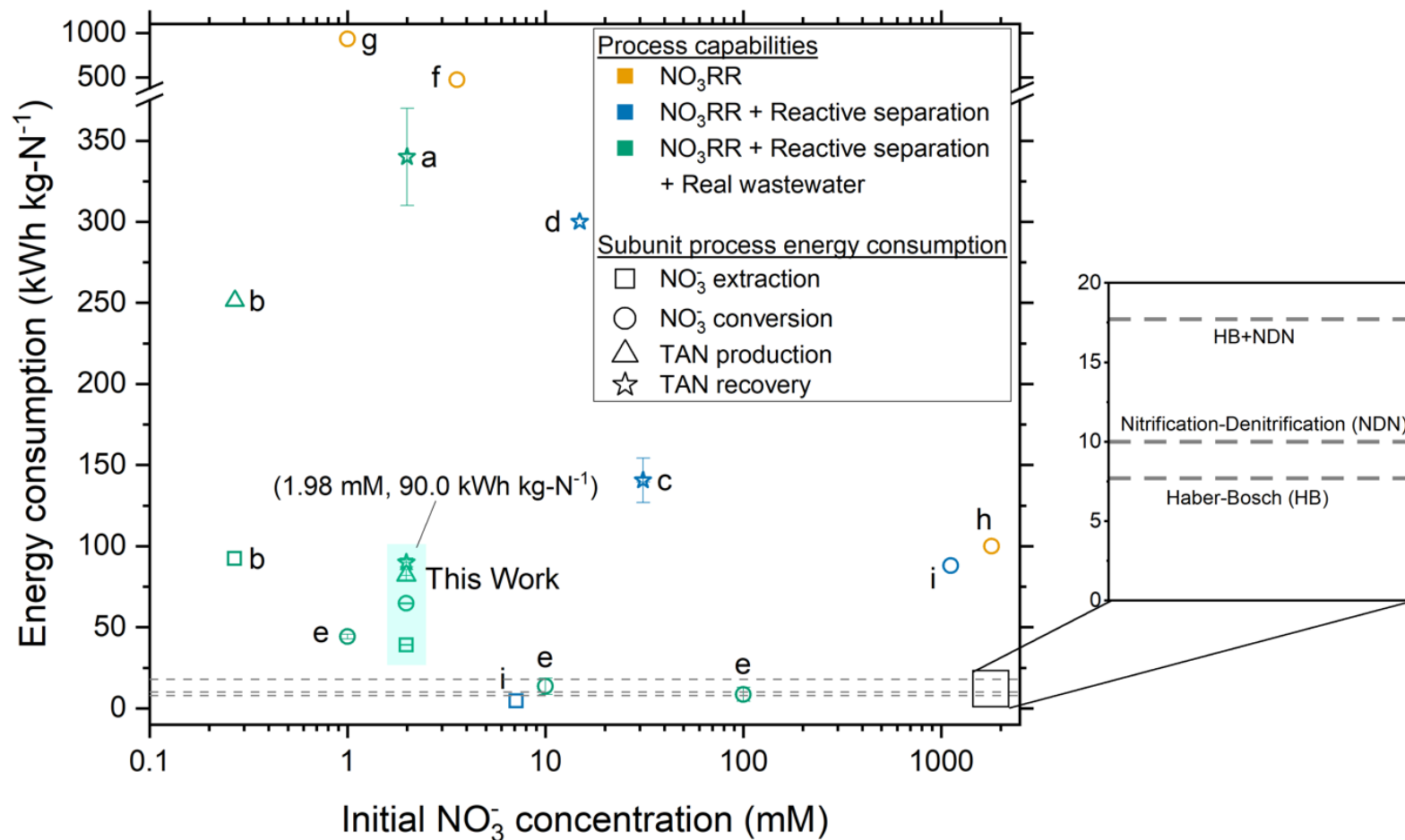
Fig. 5. Energy consumption of NO_3^- extraction, NO_3^- conversion, TAN production, and TAN recovery subunit processes for reports of reactive separations in NO₃RR literature. Error bars for This Work represent ± one standard deviation from triplicate experiments (n=3). Error bars were included as-reported for references a, c, and e. Fig. 5 shows ECaB energy consumption (kWh kg-N⁻¹) where the numerator is the same energy for all metrics and the denominator is the nitrogen mass associated with NO_3^- extraction, NO_3^- conversion, TAN production, and TAN recovery (SI

23

346   Section S5.1). Energy consumption values shown are therefore cumulative, such that a subunit process energy consumption is the sum of all

347   preceding subunit processes (i.e., TAN recovery will always be largest because it is the sum of all subunit processes). Equations used to calculate

348   energy consumption are detailed in SI Section S5.1. For proof-of-concept ECaB, NO_3^- extraction and TAN recovery do not explicitly consume

349   energy but are calculated as non-zero values here as the electrochemical energy consumed divided by the mass of nitrogen extracted or recovered,

350   respectively. References for reported values from NO_3RR studies in literature are as follows: a,[38] b,[37] c,[34] d,[35] e,[49] f,[50] g,[51] h.[52] Note that studies e, f,

351   and g were focused on removal of NO_3^- as N_2. Extended Data Tables 1-4 provide a detailed comparison of ECaB to the NO_3RR systems referenced

352   in Fig. 5. The dashed lines at indicate the energy consumption of Haber-Bosch (HB), nitrification-denitrification (NDN), and the summed energy

353   consumption of HB+NDN.

24

354   Proof-of-concept ECaB recovered a pure $(NH_4)_2SO_4$ with record low energy consumption ($90.0 \pm$

355 2.7 kWh kg-N^{-1}) for an NO$_3$RR reactive separation process (Fig. 5), due to the selectivity and FE_{TAN} of

356 Co(DIM)-mediated NO$_3$RR in relatively dilute NO_3^- ($\leq 5.8 \pm 0.2$ mM for all time points). Energy

357 consumption is a major driver of wastewater treatment technology feasibility[53] and is therefore a crucial

358 metric to compare to related systems and to incumbent processes. Proof-of-concept ECaB demonstrates

359 that its subunits (NO_3^- extraction, NO_3^- conversion, and TAN recovery; Fig. 5 symbol shape) consume a

360 proportionate amount of energy in an integrated unit process format. The cumulative energy consumption

361 was also achieved from a real wastewater using reactive separations, demonstrating robust process

362 capabilities (Fig. 5 symbol color). The cumulative energy consumption of Proof-of-concept ECaB is within

363 3.6-7.1 times that of conventional centralized nitrogen management (12.7-25.1 kWh kg-N^{-1}), consisting of

364 HB ammonia production (7.7-10.1 kWh kg-N^{-1})[54] and nitrification-denitrification (NDN) wastewater

365 treatment (5-15 kWh kg-N^{-1}).[55] Additionally, the cost of producing ammonium sulfate in ECaB is \$2.70

366 kg-N^{-1} and competitive with the retail price (\$2.75 kg-N^{-1}) if electricity is considered the only operational

367 expenditure (Section S5.1).[56] The low energy consumption and product cost in proof-of-concept ECaB are

368 promising, but the long operational timescale (96 h) is limited by the relatively slow NO_3^- conversion

369 subunit rate (Fig. S32).

370

2.2.3: ECaB Subunit Process Engineering
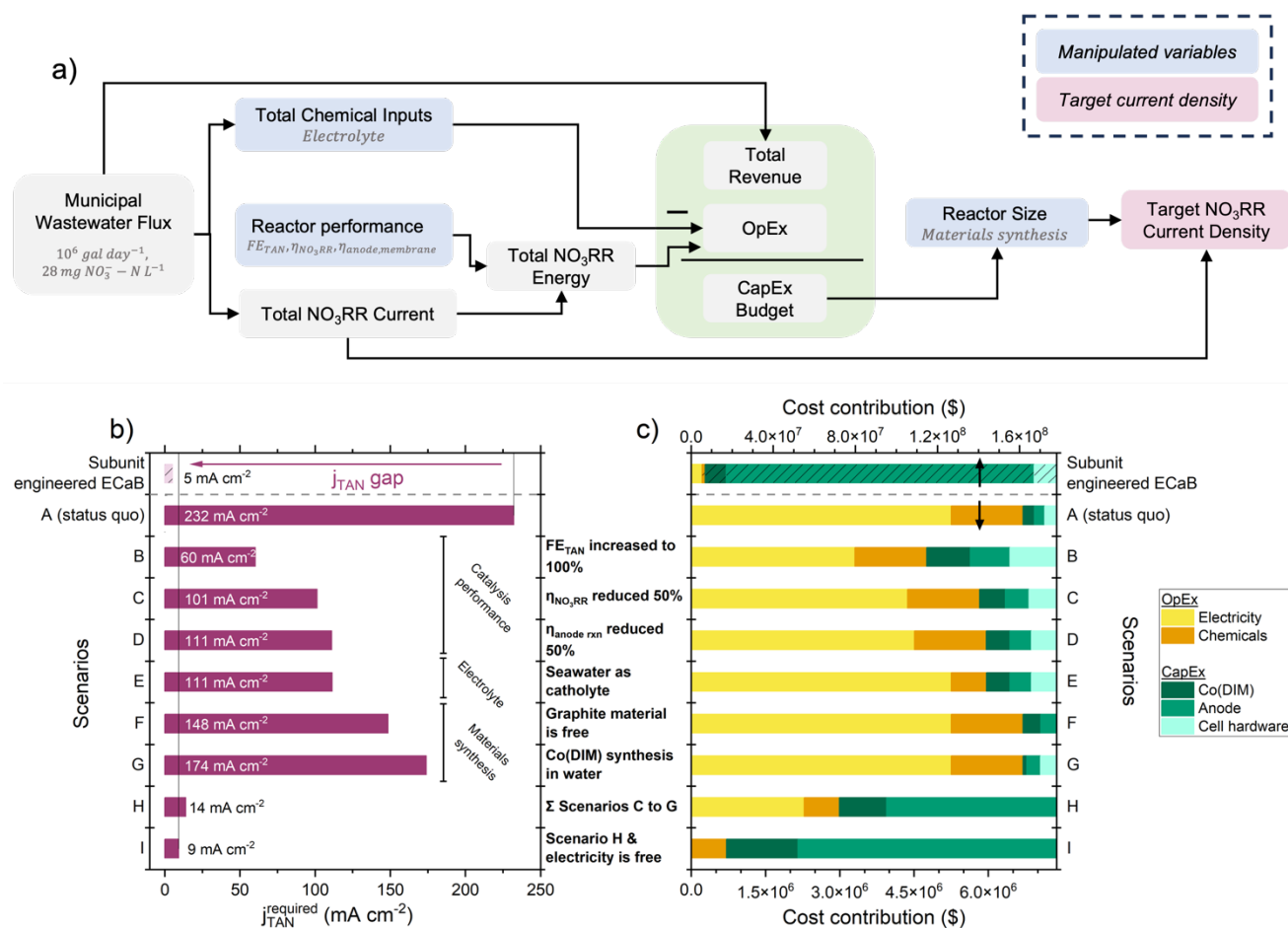
Fig. 6. (a) Flow diagram for simplified cost assessment of Co(DIM)-mediated NO_3RR in ECaB. The flux of wastewater NO_3^- from a large wastewater treatment plant (1×10^6 $gal_{wastewater}$ day^{-1})[57] was used as a basis for the operating expenditures (OpEx; chemical costs and electricity costs), capital

375 expenditure (CapEx), and revenue of a scaled-up ECaB system. The difference between the net present values of revenue and expenditures was set

376 to zero to determine the CapEx budget. The entire CapEx budget was spent on Co(DIM), anode material, and cell hardware material, which defined

377 the geometric surface area required. The total current was divided by the surface area to obtain j_{TAN}. Detailed calculation are provided in Section

378 S7.2. (b) TAN current density (j_{TAN}; red) for experimental ECaB performance (this work, Co(DIM)-ECaB) and for scenario-specific performance

379 targets. In all scenarios, the cost of electricity was ¢3 kWh^{-1}.[58] For Co(DIM)-ECaB and Scenario A, FE_{TAN} was 62.9% and E_{cell} was 2.7 V (η_{NO_3RR}

380 was 0.905 V and $\eta_{anode\ rxn}$ was 0.765, calculated from the pH-dependent equilibrium potentials of NO_3RR and OER). With improvements to catalysis

381 thermodynamic performance, electrolytes, and materials synthesis, the target current density for Co(DIM)-ECaB to be a net zero cost is decreased

382 by 16.6 times (from 232.2 mA cm^{-2} to 14.0 mA cm^{-2}). If electricity becomes a free utility, this target can be further reduced to 9.2 mA cm^{-2}. (c) Cost

383 contribution of OpEx (electricity and chemical inputs) and CapEx (Co(DIM), anodes, and cell hardware) to the overall system.

384

27

385   Because ECaB subunit processes rely on preceding subunits, the rate-limiting NO_3^- conversion

386   subunit was improved by process engineering of the preceding NO_3^- extraction step. DD equilibrium

387   calculations suggested that catholyte $[NO_3^-]$ up-concentration could exceed 100x from our 2 mM

388   wastewater-NO_3^- feed solution (Fig. S33). In subunit engineered ECaB experiments, we used a commercial

389   electrolyzer with a serpentine flow field to minimize solution-phase mass transport limitations (Fig. S34,

390   S35). This modification enabled NO_3^- extraction in subunit engineered ECaB to treat 10× the volume of

391   wastewater compared to proof-of-concept (Section 2.2.1) to below the drinking water $[NO_3^-]$ limit in the

392   same 24 h period (67.5% of NO_3^- extracted; Fig. S36, S37). The corresponding subunit engineered NO_3^-

393   extraction rate (151.6 μg-N cm^{-2} h^{-1}) was 14.6x that of proof-of-concept (Table 1, Fig. S38). The resulting

394   up-concentrated catholyte $[NO_3^-]$ was 54.4 mM, which improved the NO_3^- conversion subunit by Co(DIM)-

395   mediated NO_3RR's first order dependence on $[NO_3^-]$. Subunit engineered ECaB achieved a TAN partial

396   current density (j_{TAN}) of 5.1 mA cm^{-2} (319.6 μg-N cm^{-2} h^{-1}): 20.4× that of proof-of-concept. Improved j_{TAN}

397   enabled a TAN yield of 82.5% in only 8 h. Subunit engineered ECaB energy consumption for TAN

398   production (67.2 kWh kg-N^{-1}) is even lower than proof-of-concept ECaB (81.9 ± 3.5 kWh kg-N^{-1}, Fig.

399   S38). We thus overcame ECaB rate limitations by subunit process engineering while maintaining the proof-

400   of-concept process innovations (low energy consumption and Mg fouling prevention).

401   To quantify the performance gap between subunit engineered ECaB and operationally feasible

402   systems, we derived scenario-based j_{TAN} targets from a cost assessment of wastewater treatment coupled

403   with fertilizer production. Cost was chosen as a basis for targets because it is the largest driver of wastewater

404   treatment technology feasibility;[53] j_{TAN} was chosen as a representative performance target because it

405   influences cost[59,60] and facilitates comparisons across electrochemical systems. ECaB's primary function

406   (wastewater treatment) can be offset by its ability to recover chemical value, so we determined target j_{TAN}

407   values that would allow Co(DIM) in the ECaB system to be a net-zero cost over a ten year lifetime treating

408   wastewater NO_3^- from a large wastewater treatment plant ($1×10^6$ gal$_{wastewater}$ day^{-1})[57] (Fig. 6a, Section

409   S7.2). Our assessment is conservative because it considered revenue from $(NH_4)_2SO_4$ fertilizer but did not

28

consider other financial incentives of ECaB in a wastewater treatment process, such as water recovery revenue, conventional nitrogen treatment costs, or avoided regulatory fines for environmental NO_3^- discharge. The calculated difference between target j_{TAN} and our experimental j_{TAN} describes the gap in reactor-level catalytic activity required for ECaB process feasibility. Using the same FE_{TAN}, η_{NO_3RR}, and $\eta_{anode, membrane}$ observed in subunit engineered ECaB, the required j_{TAN} for the unit process to be a net-zero cost was 232 mA cm^{-2} (45.2x that of our experimental value; Fig. 6b). While this gap is large, it may be overcome by engineering thermodynamic performance (Scenarios B-D), electrolyte identity (Scenario E), and materials synthesis (Scenarios F-G). FE_{TAN} played the largest role in reducing target j_{TAN} and could be addressed by unit process-level development (e.g., enhancing NO_3^- up-concentration to its thermodynamic limit). Seemingly innocuous changes had large contributions to reducing target j_{TAN} (e.g., using seawater as a catholyte reduced target j_{TAN} by 52.1%). In the limit where all Scenarios B-G are achieved and electricity is a free utility (i.e., Scenario I), the target j_{TAN} is 1.8x our subunit engineered ECaB j_{TAN}. The dominant cost contribution to j_{TAN} targets in Scenarios A-G (Fig. 6c) was operational expenditures (OpEx, specifically electricity cost). Only in Scenario H, when FE_{TAN}, η_{NO_3RR}, and $\eta_{anode, membrane}$ were improved together, did capital expenditures (CapEx) outweigh OpEx. Meanwhile, Co(DIM) synthesis was a minority cost contributor in all scenarios, indicating that homogenous catalysts like Co(DIM) can be financially feasible and that efforts to reduce overall system cost should prioritize engineering reaction potentials and FEs. Practically, our cost analysis highlights that overcoming limitations of reaction thermodynamics, electrolyte engineering, and materials synthesis can significantly reduce gaps between experimental and target j_{TAN} of scalable systems.

In addition to converting wastewater NO_3^- to purified TAN at unprecedented rates and energy efficiency, ECaB also provides a generalizable, modular platform for benchmarking electrocatalysis. For example, we performed Co(DIM)-mediated nitrite reduction in ECaB with a simplified wastewater feed containing NO_2^-, achieving a TAN yield of 71.0% in 2 hours of CPE (Fig. S39). ECaB could similarly be used for CO_2 reduction (homogeneous or heterogeneous) from HCO_3^-/CO_3^{2-} feeds. The ECaB platform and

29

435   our cost assessment could be adapted to other homogeneous and heterogeneous catalysts, electrodes,

436   membranes, mass transport conditions, and operating parameters in specific wastewaters. Performing both

437   extraction and recovery via membranes facilitates comparison of co-dependent reaction and separation rates

438   and efficiencies (Extended Data Tables 1-4).[61] Volume reduction of NO_3^--containing electrolytes by low-

439   energy separations processes like DD could help remediate the majority of NO_3^- emissions contributed by

440   high volume, dilute NO_3^- sources. The combination of subunit processes in ECaB driven by only one

441   electrochemical power source will integrate well with distributed renewable power generation and storage.

442   ECaB is therefore a promising and practical platform to investigate modular and on-site reactive separations.

443

30

3. Conclusions

In this study, we elucidated catalytically influential wastewater constituents (specifically Mg^{2+}) and their effects on a homogeneous NO_3RR catalyst's (Co(DIM)) performance to rationally design a novel reactive separations process: electrocatalyst-in-a-box (ECaB). Iteratively investigating reactor-scale performance and microenvironment-scale interfacial phenomena provided design principles for a system resilient to wastewater impurities, which we systematically interrogated using simplified, simulated, and real wastewaters. The presence of Mg^{2+} in real NO_3^--bearing secondary effluent inhibited NO_3RR activity but did not affect NO_3RR selectivity or FE. Mg deposition on the cathode surface was shown to be the major passivation mechanism, aligned with recent heterogeneous NO_3RR reports of water hardness passivating cathodes.[14] Heterogeneous electron transfer between the cathode and homogeneous Co(DIM) was slowed by the passivated surface, but the homogeneous NO_3RR reaction was not observably affected. We showed that Co(DIM) can protect the cathode from inhibition by preventing specific adsorption of Mg^{2+}. We also showed that anion-selective separations via DD enable cathode protection along with homogeneous catalyst reuse and treated water recovery. Combining DD and NO_3RR within the ECaB process demonstrated promising wastewater NO_3^- extraction, NO_3^- conversion to TAN, and TAN recovery as a purified product. Proof-of-concept ECaB achieved $98.1 \pm 0.3\%$ NO_3^--N removal from a real municipal secondary effluent and recovered a pure TAN product with the lowest reported energy consumption to date for an NO_3RR system (90.0 ± 2.7 kWh kg-N^{-1}). Subunit engineered ECaB enabled a sustained j_{TAN} of 5.14 mA cm$^{-2}_{geometric}$ for 8 h of Co(DIM)-mediated NO_3RR with low energy consumption maintained (67.2 kWh kg-N^{-1} for TAN production). A cost assessment showed that subunit engineered ECaB j_{TAN} must be improved by 45.2× to meet status-quo performance targets, but that tractable improvements to catalysts, electrolytes, and materials in ECaB systems can reduce targets to 1.8× the j_{TAN} we achieved in subunit engineered ECaB.

This work encourages the use-informed study of molecular catalysts and integrated unit process analysis for wastewater refining. The development of ECaB was informed entirely by the composition of a

31

469 generalizable NO_3^--rich wastewater, underscoring the imperative connection between wastewater-based

470 electrochemical research and the value propositions posed by a unit process. The developed ECaB

471 architecture can also serve as a platform for investigating wastewaters, catalysts, and reactor operating

472 conditions. Deployment feasibility for NO_3RR reactive separations systems will be governed by analysis

473 of efficiencies, rates, and energy consumption for extraction, conversion, and recovery unit processes.[62]

474 The study of integrated reactive separations that match the scale of wastewater-NO_3^- generation will

475 accelerate use of wastewaters as feedstocks for electrified chemical production. Ultimately, this work

476 innovates on incumbent centralized nitrogen management systems by producing commodities from impure,

477 variable, and complex NO_3^--rich wastewaters.

478

4.1 Tables

480 **Table 1.** Summary of performance metrics for the proof-of-concept and subunit engineered ECaB iterations.

| Metric	Subunit	Proof-of-concept ECaB	Subunit engineered ECaB
Operation time (h)	NO_3^- Extraction	96 h	24 h
	TAN Production	30 h	8 h
	TAN Recovery	72 h	24 h
	Total	96 h	48 h
Rate ($\mu g\ N\ cm^{-2} h^{-1}$)	NO_3^- Extraction	10.4 ± 0.1	151.6
	TAN Production	15.7 ± 0.9	319.6
	TAN Recovery	6.0 ± 0.2	45.8
Energy consumption ($kWh\ kg\ N^{-1}$)	NO_3^- Extraction	0 (39.0 ± 0.2 considering all subunits)	0 (48.2 considering all subunits)
	TAN Production	81.9 ± 3.5	67.2
	TAN Recovery	90.0 ± 2.7	295.3
Efficiency (%)	NO_3^- Extraction ($\eta_{NO_3^- Extraction}$)	$98.1 \pm 0.3\%$	67.5%
	TAN Production (Y_{TAN})	$49.0 \pm 2.6\%$	82.5%
	TAN Recovery ($\eta_{TAN\ Recovery}$)	$91.0 \pm 2.1\%$	22.8%

481

482 **4.2. Extended Data Figures**
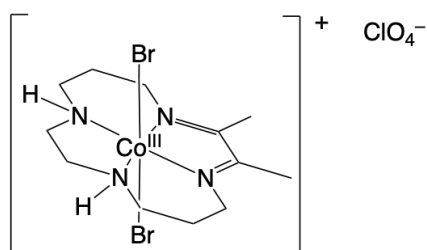
483

484 **Extended Data Fig. 1.** The structure of Co(DIM) in its synthesized, crystalline form.

485

33
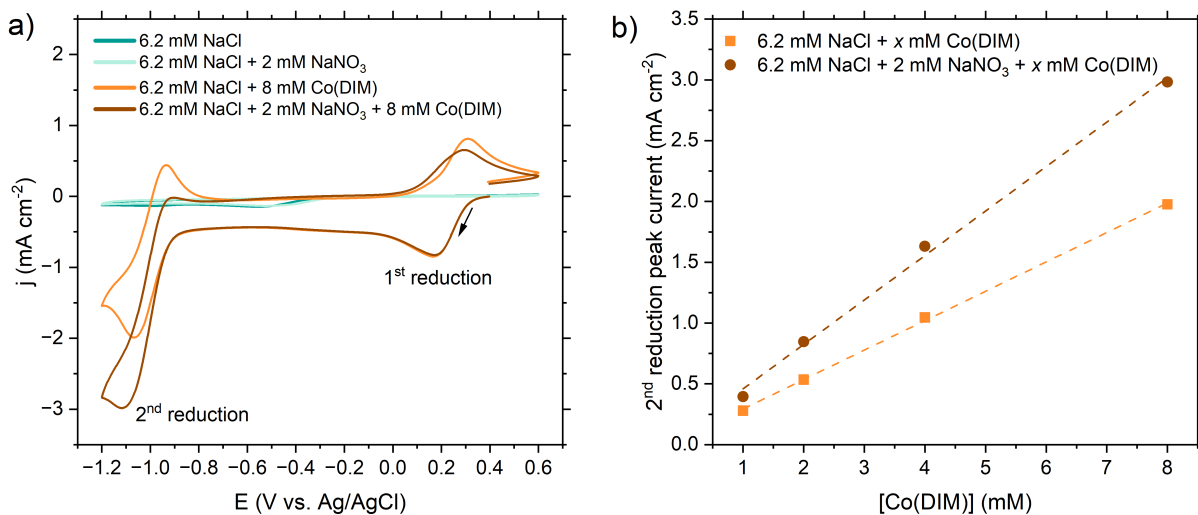
Extended Data Fig. 2. (a) Cyclic voltammograms collected in 6.2 mM NaCl (background electrolyte matching the Cl⁻ concentration in real wastewater), 6.2 mM NaCl with 2 mM NaNO₃ (background electrolyte with representative nitrate concentration), 6.2 mM NaCl with 8 mM Co(DIM) (background electrolyte with catalyst), and 6.2 mM NaCl with 2 mM NaNO₃ and 8 mM Co(DIM) (background electrolyte with catalyst and representative nitrate concentrations). Working electrode: 5 mm GC disk. Counter electrode: 6.4 mm graphite rod. Reference electrode: Ag/AgCl (4.0 M KCl). Scan rate: 100 mV s⁻¹. (b) Peak current density of the second reduction peak (~ –1.1 V vs. Ag/AgCl) of 6.2 mM NaCl with 8 mM Co(DIM) in the presence and absence of 2 mM NaNO₃. Associated voltammograms are provided in Fig. S4. The excess factor, defined as the concentration of substrate (NO₃⁻) divided by the concentration of catalyst (Co(DIM)), ranged from 2 to 200 previously. To address dilute real wastewaters, we minimized the excess factor with 8 mM Co(DIM) (the observed solubility limit at room temperature) to maximize NO₃RR activity (excess factor 0.25, Fig. 1b). Without Co(DIM), the GC working electrode is inactive for NO₃RR (NaCl and NaCl + NaNO₃ curves). In the presence of Co(DIM), two reversible redox peaks exist, the first at $E_{1/2}$ = +0.24 V vs. Ag/AgCl and the second at $E_{1/2}$ = –1.00 V vs. Ag/AgCl. With both Co(DIM) and NO₃⁻ in solution, catalysis is evidenced by an increased current density (i.e., catalytic current) of the second reductive wave and loss of reversibility on the reverse (anodic) scan. Catalytic current is caused by a local enrichment of [Co(DIM)] during heterogeneous activation and homogeneous NO₃RR in the

34

504   reaction-diffusion layer (RDL).[39] With higher Co(DIM) concentration (i.e., lower excess factor), the second

505   reduction peak current increases linearly both in the presence and absence of NO_3^- (Fig. 1c, Fig. S4)

506 **4.3. Extended Data Tables**

507 **Extended Data Table 1**. Efficiency, rate, and energy comparison to literature: Nitrate extraction

ref	Wastewater	Extraction mechanism	Nitrate extraction efficiency ($\eta_{NO_3^- Extraction}$)	Nitrate extraction rate		Nitrate extraction energy consumption
				$\mu g\ N\ cm^{-2} h^{-1}$	$mg\ N\ L^{-1} day^{-1}$	kWh kg-N^{-1}
*This work	Secondary effluent (2 mM nitrate)	Donnan dialysis (1 M KCl receiver solution)	81.3 ± 3.3% at 24 h 98.1 ± 0.3% at 96 h	34.6 ± 1.7 at 24 h 10.4 ± 0.1 at 96 h	23.0 ± 1.3 at 24 h 7.8 ± 0.1 at 96 h	0 (39.0 ± 0.2 considering all subunits)
*This work	Secondary effluent (2 mM nitrate)	Donnan dialysis (1 M KCl receiver solution)	67.5% at 24 h	151.6 at 24 h	18.2 at 24 h	0 (48.2 considering all subunits)
38	Secondary effluent (2 mM nitrate)	n/a				
37	Agricultural tile drainage (0.27 mM nitrate)	Electrodeionization with Polyaniline-Co$_3$O$_4$-carbon nanotube slurry coated on Ti mesh as electrode	n.r.	n.r.	n.r.	92.2
35	25 mM NaNO$_3$ in 0.1 M Na$_2$SO$_4$	n/a				
	Printing wastewater (14.9 mM nitrate)	n/a				
34	*25 mM NaNO$_3$ in 0.5 M Na$_2$SO$_4$*	n/a				
	Pharmaceutical industry wastewater (31.1 ± 1.1 mM nitrate)	n/a				
36	Oil refining & chemical catalyst manufacturing wastewater (36.1 ± 0.9 mM nitrate)	n/a				
63	*7.14 mM KNO$_3$*	Electrodialysis, 5 cm^2 (2 M KNO$_3$ receiver solution)	75.0%	542.4	n.r.	n.r.

508 *Equations used to calculate ECaB performance metrics in this work are provided in Section S.5.1.

509 **Extended Data Table 2**. Efficiency, rate, and energy comparison to literature: Nitrate conversion by NO₃RR

ref	Wastewater	Electrode/catalyst (Geometric surface areas)	Nitrate conversion ($\chi_{NO_3^- \; Conversion}$)	FE to TAN	Nitrate conversion rate		Nitrate conversion energy consumption
					$\mu g \; N \; cm^{-2}_{geometric} h^{-1}$	$mg \; N \; L^{-1} day^{-1}$	$kWh \; kg\text{-}N^{-1}$
*This work	Secondary effluent (2 mM nitrate concentrated to 5.8 mM)	Co(DIM), 5.4 cm² glassy carbon plate cathode	62.0 ± 1.0% at 96 h (30 h cumulative CPE)	57.4 ± 0.2% at 96 h (30 h cumulative CPE)	20.0 ± 0.2 at 96 h (30 h cumulative CPE)	59.1 ± 1.9 at 96 h (30 h cumulative CPE)	64.7 ± 0.4 cumulative at 96 h (30 h CPE)
*This work	Secondary effluent (2 mM nitrate concentrated to 54 mM)	Co(DIM), 10 cm² graphite serpentine flow field	80.8 at 48 h (8 h cumulative CPE)	62.9 % at 48 h (8 h cumulative CPE	329.0 at 48 h (8 h cumulative CPE	2193.5 at 48 h (8 h cumulative CPE	66.6 cumulative at 48 h (8 h CPE
38	Secondary effluent (2 mM nitrate)	Co(DIM), 64 cm² 316 SS mesh cathode	70.5 ± 2.7% at 42 h	10-15%	1.9	21	n.r.
37	Agricultural tile drainage (0.27 mM nitrate concentrated to 2.45 mM)	Polyaniline-Co₃O₄-carbon nanotube slurry coated on Ti mesh	n.r.	28%	n.r.	n.r.	n.r.
35	25 mM NaNO₃ in 0.1 M Na₂SO₄	Electrodeposited Co on Ti mesh (16 cm²)	100% at 3 h	43.7%	n.r.	n.r.	n.r.
	Printing wastewater (14.9 mM nitrate)	Electrodeposited Co on Ti mesh (16 cm²)	100% at 3 h	n.r.	n.r.	n.r.	n.r.
34	*25 mM NaNO₃ in 0.5 M Na₂SO₄*	CuO@Cu foam	~100%	49.2%	1846 ± 46	n.r.	n.r.
	Pharmaceutical industry wastewater (31.1 ± 1.1 mM nitrate)	CuO@Cu foam	>96.9%	n.r.	1817 ± 75	n.r.	n.r.
36	Oil refining & chemical catalyst manufacturing wastewater (36.1 ± 0.9 mM nitrate)	Ni foam (1.4 m²)	95%	n.r.	n.r.	n.r.	n.r.

37

63	*1.12 M KNO₃ in 60 wt% NaOH/KOH*	Ni mesh (100 cm^2), 80 °C	n.r.	70.4%	n.r.	n.r.	n.r.

510   *Equations used to calculate ECaB performance metrics in this work are provided in Section S.5.1.

511

38

Extended Data Table 3. Efficiency, rate, and energy comparison to literature: TAN production by NO$_3$RR

ref	Wastewater	Electrode/catalyst (Geometric surface areas)	NO$_3$RR product	TAN yield (Y_{TAN})	TAN yield rate		TAN production energy consumption
					$\mu g\ N\ cm^{-2}h^{-1}$	$mg\ N\ L^{-1}day^{-1}$	kWh kg-N^{-1}
*This work	Secondary effluent (2 mM nitrate concentrated to 5.8 mM)	Co(DIM), 5.4 cm^2 glassy carbon plate cathode	TAN in 1 M KCl	49.0 ± 2.6% at 96 h (30 h cumulative CPE)	15.7 ± 0.9 at 96 h (30 h cumulative CPE)	46.2 ± 0.8 at 96 h (30 h cumulative CPE)	81.9 ± 3.5 cumulative at 96 h (30 h CPE)
*This work	Secondary effluent (2 mM nitrate concentrated to 54 mM)	Co(DIM), 10 cm^2 graphite serpentine flow field	TAN in 1 M KCl	82.5 at 48 h (8 h cumulative CPE)	319.6 at 48 h (8 h cumulative CPE)	2130.6 at 48 h (8 h cumulative CPE)	67.2 cumulative at 48 h (8 h CPE)
38	Secondary effluent (2 mM nitrate)	Co(DIM), 64 cm^2 316 SS mesh cathode	TAN in secondary effluent	n.r.	n.r.	n.r.	n.r.
37	Agricultural tile drainage (0.27 mM nitrate concentrated to 2.45 mM)	Polyaniline-Co$_3$O$_4$-carbon nanotube slurry coated on Ti mesh	TAN in 0.1 M NaCl	n.r.	89.0	n.r.	159.1 for NO$_3$RR (251.3 including extraction)
35	*25 mM NaNO$_3$ in 0.1 M Na$_2$SO$_4$*	Electrodeposited Co on Ti mesh (16 cm^2)	TAN in NaNO$_3$ and 0.1 M Na$_2$SO$_4$	n.r.	n.r.	n.r.	n.r.
	Printing wastewater (14.9 mM nitrate)	Electrodeposited Co on Ti mesh (16 cm^2)	TAN in printing wastewater	n.r.	n.r.	n.r.	n.r.
34	25 mM NaNO$_3$ in 0.5 M Na$_2$SO$_4$	CuO@Cu foam	TAN in NaNO$_3$ and 0.5 M Na$_2$SO$_4$	n.r.	n.r.	n.r.	n.r.
	Pharmaceutical industry wastewater (31.1 ± 1.1 mM nitrate)	CuO@Cu foam	TAN in NaNO$_3$ and 0.5 M Na$_2$SO$_4$	n.r.	n.r.	n.r.	n.r.
36	Oil refining & chemical catalyst manufacturing wastewater (36.1 ± 0.9 mM nitrate)	Ni foam (1.4 m^2)	TAN in manufacturing wastewater	n.r.	n.r.	n.r.	n.r.

| 63 | *1.12 M KNO₃ in 60 wt% NaOH/KOH* | Ni mesh (100 cm²), 80 °C | TAN in 60 wt% NaOH/KOH | n.r. | 11494 | n.r. | 83.4 for NO₃RR (does not include extraction) |

513   *Equations used to calculate ECaB performance metrics in this work are provided in Section S.5.1.

514 **Extended Data Table 4**. Efficiency, rate, and energy comparison to literature: TAN recovery

ref	Wastewater	Recovery mechanism	Recovered product	TAN recovery efficiency ($\eta_{TAN\ Recovery}$)	TAN recovery rate		TAN recovery energy consumption
					$\mu g\ N\ cm^{-2}h^{-1}$	$mg\ N\ L^{-1}day^{-1}$	kWh kg-N^{-1}
*This work	Secondary effluent (2 mM nitrate concentrated to 5.8 mM)	Electrochemical basification + Membrane stripping (5.4 cm^2 membrane area)	$(NH_4)_2SO_{4,aq}$ in 0.1 M $H_2SO_{4,\ aq}$	$91.0 \pm 2.1\%$ at 96 h (*Overall N recovery: $42.6 \pm 1.4\%$)	6.0 ± 0.2 at 96 h	18.1 ± 0.2 at 96 h	90.0 ± 2.7 at 96 h (cumulative)
*This work	Secondary effluent (2 mM nitrate concentrated to 54 mM)	Electrochemical basification + Membrane stripping (5.4 cm^2 membrane area)	$(NH_4)_2SO_{4,aq}$ in 0.1 M $H_2SO_{4,\ aq}$	22.8% at 48 h (*Overall N recovery: 11.0%)	45.8 at 48 h	169.6 at 48 h	295.3 at 48 h (cumulative)
38	Secondary effluent (2 mM nitrate)	Electrochemical basification + Membrane stripping (64 cm^2 membrane area)	$(NH_4)_2SO_{4,aq}$ in 0.1 M $H_2SO_{4,\ aq}$	Overall N recovery: $53.6 \pm 2.8\%$	1.3	15.9	340 ± 30 (cumulative)
37	Agricultural tile drainage (0.27 mM nitrate concentrated to 2.45 mM)	n/a					
35	*25 mM NaNO₃ in 0.1 M Na₂SO₄*	Electrochemical basification + Membrane stripping (16 cm^2 membrane area)	$(NH_4)_2SO_{4,aq}$ in 1 M $H_2SO_{4,\ aq}$	Overall N recovery: 83.8% at 3 h	n.r.	n.r.	155
	Printing wastewater (14.9 mM nitrate)	Electrochemical basification + Membrane stripping (16 cm^2 membrane area)	$(NH_4)_2SO_{4,aq}$ in 1 M $H_2SO_{4,\ aq}$	Overall N recovery: 86% at 3 h	n.r.	n.r.	n.r.
34	25 mM NaNO₃ in 0.5 M Na₂SO₄	Electrochemical basification + Membrane stripping (4 cm^2 membrane area)	$(NH_4)_2SO_{4,aq}$ in acidified 0.5 M Na₂SO$_{4,\ aq}$	Overall N recovery: ~100%	733 ± 42	n.r.	140.6 ± 13.7
	Pharmaceutical industry wastewater (31.1 ± 1.1 mM nitrate)	Electrochemical basification + Membrane stripping (4 cm^2 membrane area)	$(NH_4)_2SO_{4,aq}$ in acidified 0.5 M Na₂SO$_{4,\ aq}$	n.r.	916 ± 27	n.r.	n.r.
36	Oil refining & chemical catalyst manufacturing	n/a					

41

	wastewater (36.1 ± 0.9 mM nitrate)						
63	*1.12 M KNO₃ in 60 wt% NaOH/KOH*	Carrier gas stripping	$NH_{3,(aq)}$, NH_4HCO_3, $(NH_4)_2SO_4$	~100%	n.r.	n.r.	n.r.

515   *Equations used to calculate ECaB performance metrics in this work are provided in Section S.5.1.

5. Methods

All chemicals were purchased as reagent grade and used as received. Nanopure water (resistivity: 18.2 MΩ·cm) was used for all experiments and measurements unless stated otherwise. Before experiments, cation exchange membranes (CEM; CMI-7000, Membranes International Inc.) were stored in 0.1 M $KClO_4$; anion exchange membranes (AEM; ASVN, Selemion) were stored in nanopure water; and bipolar membranes (BPM; FBM, Fumasep) were stored in 1 M NaCl. Hydrophobic gas-permeable membranes (GPM; CLARCOR QP 952 (polytetrafluoroethylene), CLARCOR Industrial Air) were used as received.

5.1. Catalyst synthesis and characterization

The perchlorate salt of $[Co(DIM)Br_2]^+$ (Fig. 1a) was prepared as detailed previously.[28] ^{1}H NMR spectra (Varian Inova 600 at 600 MHz; Fig. S1) and LC-MS spectra (Agilent 1260 HPLC with an Agilent 6460 Triple Quadrupole MS; Fig. S2) of Co(DIM) confirmed the anticipated structure (Extended Data Fig. 1), molecular weight, and axial ligation of the catalyst.

5.2. Electrochemical methods

A BioLogic VMP-300 potentiostat was used to control the potential applied to the working electrode versus the reference electrode. All electrochemical experiments were recorded using 85% IR compensation based on the ohmic resistance obtained via potentiostatic electrochemical impedance spectroscopy.

5.2.1. Cyclic voltammetry (CV) and rotating-disk electrode (RDE) controlled-potential electrolysis (CPE)

All CV and RDE CPE experiments were conducted in a 5-port glass RDE cell (Pine Research). The working electrode was a 5 mm glassy carbon (GC) disk (Pine Research), the counter electrode was a 6.4 mm diameter graphite rod in a glass tube with a Teflon frit (Pine Research), and the reference electrode was a Ag/AgCl electrode (Pine Research, 4.0 M KCl). The 5 mm GC electrode was polished with 1 μm alumina slurry (BASi) in a figure-eight motion on a microcloth polishing pad (BASi) for one minute. After polishing, the GC electrode was sonicated in nanopure water for one minute and blown dry with N_2. All CVs were collected at 100 mV/s and the first sweep of each CV is shown. All CVs began at the open circuit

541 potential (OCP) and were swept to the first switching potential of –1.2 V vs. Ag/AgCl, then swept to the

542 second switching potential of +0.6 V vs. Ag/AgCl, then swept back to OCP. RDE CPEs were performed

543 using an electrode rotator (Pine Research). During dosing experiments, 28 μL of 1 M $MgCl_2$, 30 μL of 1 M

544 $NaHCO_3$, or 38 μL of 1 M $CaCl_2$ were manually pipetted into 20 mL of electrolyte via a glass port in the

545 cell. The injected volumes of 1 M salt solutions were such that each species (Mg^{2+}, Ca^{2+}, HCO_3^-)

546 concentration in the 20 mL of electrolyte matched the concentration in the real wastewater.

547 <u>5.2.2. Two-chamber controlled-potential electrolysis (CPE)</u>

548 Two-chamber CPE experiments were performed in a polycarbonate compression cell separated by

549 a CEM and held together with stainless steel bolts. Each chamber had a volume of ~7 mL and a chamber

550 cross-sectional area of 5.4 cm^2. The working electrode (cathode) was a type II GC plate (ThermoFisher

551 Scientific) and was stored in 1 M H_2SO_4 when not in use to remove any trace metal impurities. Before CPE,

552 the GC electrode was prepared in the same manner as described in Section 5.2.1. The counter electrode

553 (anode) was a mixed metal oxide (MMO) iridium-tantalum mesh (Titan Metal Fabricators). The geometric

554 cross-sectional area of the cathode, anode, and CEM were 5.4 cm^2. The reference electrode was a leakless

555 Ag/AgCl electrode (3.4 M KCl; ET072, eDAQ) calibrated against a master reference electrode (4.0 M KCl;

556 Fisherbrand accumet) and was inserted into the cathode chamber via a threaded port. Three catholytes were

557 tested: simplified wastewater, simulated wastewater, and real wastewater (Table S1). The anolyte was 0.1

558 M $KClO_4$ in all experiments. 50 mL of each electrolyte were recirculated in batch at a volumetric flow rate

559 of 3.5 mL min^{-1} (linear flow rate in each chamber: 1.75 cm min^{-1}) to match our previous investigation of

560 Co(DIM).[38] Buffers were not used in CPE because previous investigations showed that Co(DIM)-mediated

561 NO_3RR catalysis is inhibited by common inorganic (phosphate, carbonate/bicarbonate) buffers;[27] we also

562 tried common "non-coordinating" buffers (TRIS, MOPS, borax) but observed no catalysis in CV or CPE.

563 The statistical significance of differences between observed CPE performance in the three

564 catholytes was compared using paired t-tests for equal means, where we rejected the null hypothesis

565 (difference between CPE performance results from a normal distribution with mean equal to zero and

566 unknown variance) if $p < 0.05$.

44

567   Rinse tests were performed to assess the catalytic activity of deposits on GC cathodes. The cell was

568   then reconstructed with the deposit-containing GC electrode. An eight-hour CPE was performed (identical

569   operation to first CPE) with 50 mL simplified wastewater without dissolved Co(DIM) in the catholyte (i.e.,

570   0 mM Co(DIM), 6.2 mM NaCl, 2 mM $NaNO_3$).

571   <u>5.2.3. Proof-of concept electrocatalyst-in-a-box (ECaB)</u>

572   The ECaB reactor consisted of two compression cells: a two-chamber cell for electrocatalysis and

573   a three-chamber cell for Donnan dialysis and ammonia gas stripping (Fig. S3). The compression cell pieces

574   were the same as used in two-chamber CPE experiments. Four electrolyte reservoirs (200 mL wastewater,

575   50 mL catholyte, 50 mL trap solution, and 50 mL anolyte) were recirculated in batch mode through the two

576   cells. The only solution to recirculate between both cells was the catholyte to facilitate the three subunit

577   processes of NO_3^--extraction by Donnan dialysis, NO_3^--conversion to TAN by Co(DIM)-mediated NO_3RR,

578   and TAN recovery by membrane stripping. In the Donnan dialysis and ammonia gas stripping cell, the

579   wastewater and catholyte were separated by an AEM (to facilitate NO_3^- extraction) and the catholyte and

580   trap solution were separated by a GPM (to facilitate TAN recovery). The electrocatalysis cell contained a

581   GC plate cathode (to facilitate NO_3^- conversion to TAN), a MMO anode, and a leakless reference electrode;

582   the catholyte and anolyte were separated by a BPM. The flow rate was 3.5 mL/min for the electrocatalysis

583   cell , and the flow rate was 28 mL/min for the Donnan dialysis and ammonia gas stripping cell. During

584   ECaB operation, the electrocatalytic cell was alternated between open circuit (0-24 h, 34-48 h, 58-72 h, 82-

585   96 h) and -1.05 $V_{Ag/AgCl}$ (24-34 h, 48-58 h, 72-82 h).

586   <u>5.2.4. Subunit engineered ECaB</u>

587   In a second iteration of ECaB experiments, a commercial serpentine flow field electrolyzer (Fuel

588   Cell Technologies, 10 cm^2) was used for both Donnan dialysis and electrocatalysis. Donnan dialysis was

589   performed first in the electrolyzer; then the electrolyzer was disassembled and reassembled to perform

590   electrocatalysis. In Donnan dialysis, an AEM was sandwiched between the two graphite flow field blocks.

591   2 L of municipal secondary effluent was used as the wastewater feed and 50 mL of 1 M KCl with 8 mM

592   Co(DIM) was used as the receiving solution. The flow rate was 57 mL/min. In electrocatalysis, a CEM was

593   sandwiched between the graphite flow field blocks and a pseudo reference electrode (a 250 μm Ag wire

594   anodized in saturated KCl) was attached to the CEM. The graphite flow block was used as the cathode. The

595   anode was a platinized Ti mesh (Fuel Cell Store) in electrical contact with the anode graphite flow block.

596   The catholyte was the resulting solution from Donnan dialysis and the anolyte was 50 mL of 0.1 M $KClO_4$.

597   The flow rate was 3.5 mL min^{-1} in the electrolyzer. –1.05 V vs. Ag/AgCl was applied in 1 hour increments.

598   After each increment, the catholyte was adjusted back to pH 6 with ~200 μL 10 wt% HCl to keep Co(DIM)

599   in its stable operating pH regime.[27,38] A separate two-chamber 5.4 cm^2 compression cell was assembled to

600   house the GPM for TAN recovery with 50 mL of 0.1 M H_2SO_4 as the trap solution; TAN recovery was run

601   in parallel with electrocatalysis at a flow rate of 28 mL/min.

602   *5.3 Aqueous characterization*

603   Aqueous ion speciation was quantified with cation chromatography (Na^+, NH_4^+, K^+, Ca^{2+}, Mg^{2+})

604   and anion chromatography (Cl^-, NO_2^-, NO_3^-, SO_4^-, PO_4^{3-}). Both cation chromatography (4 mM tartaric acid/2

605   mM oxalic acid eluent, SCS 1 column at 30 °C) and anion chromatography (4.5 mM carbonate/0.8 mM

606   bicarbonate eluent, AS23-4 μm column at 30 °C) were performed with a dual Dionex ICS-6000 system

607   (ThermoFisher Scientific). For ECaB, the high concentration of K^+ in the catholyte made quantification of

608   TAN by cation chromatography difficult, so flow injection analysis (indophenol method) was conducted

609   with a SEAL AA500 AutoAnalyzer .[38] For both cation chromatography and flow injection analysis, aliquots

610   above pH 7 were acidified to prevent ammonia volatilization and facilitate accurate quantification of

611   measure total ammonia nitrogen (TAN: sum of aqueous ammonium, NH_4^+, and aqueous ammonia, NH_3).

612   Inductively coupled plasma mass spectrometry (ICP-MS) was used to quantify the concentration of ^{59}Co in

613   each ECaB chamber at initial and final time points. ICP-MS (ThermoFisher Scientific) was performed using

614   a parallel flow nebulizer (Burgener PEEK Mira Mist) and a Peltier-cooled Scott-type double pass cyclonic

615   spray chamber cooled to 2.7 °C.[64]

616   *5.4. Electrode characterization*

617   X-ray photoelectron spectroscopy (XPS) was performed using a Phi Versaprobe 3 with

618   monochromatized Al Kα (1486 eV) radiation. Scanning electron microscopy (SEM) and energy dispersive

619   X-ray spectroscopy (EDS) characterization was performed on a Thermo Fisher Scientific Apreo S LoVac

620   (5 kV, 5.0 pA) with a Bruker Quantax EBSD 400i integrated system containing an XFlash 6|60 SDD EDS

621   detector. Raw EDS data were processed and plotted with Bruker's ESPRIT software.

622   *5.5. Efficiency, rate, and energy comparison to literature*

623   The scope of our comparison to precedent literature was constrained to literature studies that

624   investigated reactive separations in real wastewaters. Reported values of efficiencies, rates, and energy

625   consumption are shown for the four subunit processes of nitrate extraction (Extended Data Table 1), nitrate

626   conversion by NO_3RR (Extended Data Table 2), TAN production by NO_3RR (Extended Data Table 3), and

627   TAN recovery (Extended Data Table 4). Efficiencies, rates, and energy consumption were shown by Kogler

628   and co-workers to be the most important operational metrics for wastewater treatment practitioners to make

629   technology decisions for future systems.[48]

630

47

Supplementary Information

Supplementary Figs. S1-S39, Tables S1-S2, and Equations S3.1.1-7.2.1.

5. References

(1) Smith, C.; Hill, A. K.; Torrente-Murciano, L. Current and Future Role of Haber–Bosch Ammonia in a Carbon-Free Energy Landscape. *Energy Environ. Sci.* **2020**, *13* (2), 331–344. https://doi.org/10.1039/C9EE02873K.

(2) Lim, J.; Fernández, C. A.; Lee, S. W.; Hatzell, M. C. Ammonia and Nitric Acid Demands for Fertilizer Use in 2050. *ACS Energy Lett.* **2021**, *6* (10), 3676–3685. https://doi.org/10.1021/acsenergylett.1c01614.

(3) Comer, B. M.; Fuentes, P.; Dimkpa, C. O.; Liu, Y.-H.; Fernandez, C. A.; Arora, P.; Realff, M.; Singh, U.; Hatzell, M. C.; Medford, A. J. Prospects and Challenges for Solar Fertilizers. *Joule* **2019**, *3* (7), 1578–1605. https://doi.org/10.1016/j.joule.2019.05.001.

(4) Miller, D. M.; Abels, K.; Guo, J.; Williams, K. S.; Liu, M. J.; Tarpeh, W. A. Electrochemical Wastewater Refining: A Vision for Circular Chemical Manufacturing. *J. Am. Chem. Soc.* **2023**, *145* (36), 19422–19439. https://doi.org/10.1021/jacs.3c01142.

(5) *The Challenge of Tracking Nutrient Pollution 2,300 Miles | U.S. Geological Survey*. https://www.usgs.gov/news/challenge-tracking-nutrient-pollution-2300-miles (accessed 2022-02-04).

(6) Lang, M.; Li, P.; Yan, X. Runoff Concentration and Load of Nitrogen and Phosphorus from a Residential Area in an Intensive Agricultural Watershed. *Science of The Total Environment* **2013**, *458–460*, 238–245. https://doi.org/10.1016/j.scitotenv.2013.04.044.

(7) Kato, T.; Kuroda, H.; Nakasone, H. Runoff Characteristics of Nutrients from an Agricultural Watershed with Intensive Livestock Production. *Journal of Hydrology* **2009**, *368* (1), 79–87. https://doi.org/10.1016/j.jhydrol.2009.01.028.

(8) Eghball, B.; Gilley, J. E. Phosphorus and Nitrogen in Runoff Following Beef Cattle Manure or Compost Application. *Journal of Environmental Quality* **1999**, *28* (4), 1201–1210. https://doi.org/10.2134/jeq1999.00472425002800040022x.

(9) McLay, C. D. A.; Dragten, R.; Sparling, G.; Selvarajah, N. Predicting Groundwater Nitrate Concentrations in a Region of Mixed Agricultural Land Use: A Comparison of Three Approaches. *Environmental Pollution* **2001**, *115* (2), 191–204. https://doi.org/10.1016/S0269-7491(01)00111-7.

49

674   (10) Hubbard, R. K.; Sheridan, J. M. Water and Nitrate-Nitrogen Losses From a Small, Upland, Coastal

675   Plain Watershed. *Journal of Environmental Quality* **1983**, *12* (2), 291–295.

676   https://doi.org/10.2134/jeq1983.00472425001200020028x.

677   (11) Wang, Z.-H.; Li, S.-X. Chapter Three - Nitrate N Loss by Leaching and Surface Runoff in Agricultural

678   Land: A Global Issue (a Review). In *Advances in Agronomy*; Sparks, D. L., Ed.; Academic Press, 2019;

679   Vol. 156, pp 159–217. https://doi.org/10.1016/bs.agron.2019.01.007.

680   (12) McEnaney, J. M.; Blair, S. J.; Nielander, A. C.; Schwalbe, J. A.; Koshy, D. M.; Cargnello, M.; Jaramillo,

681   T. F. Electrolyte Engineering for Efficient Electrochemical Nitrate Reduction to Ammonia on a

682   Titanium Electrode. *ACS Sustainable Chem. Eng.* **2020**, *8* (7), 2672–2681.

683   https://doi.org/10.1021/acssuschemeng.9b05983.

684   (13) Bae, S.-E.; Stewart, K. L.; Gewirth, A. A. Nitrate Adsorption and Reduction on Cu(100) in Acidic

685   Solution. *J. Am. Chem. Soc.* **2007**, *129* (33), 10171–10180. https://doi.org/10.1021/ja071330n.

686   (14) Atrashkevich, A.; Fajardo, A. S.; Westerhoff, P.; Walker, W. S.; Sánchez-Sánchez, C. M.; Garcia-

687   Segura, S. Overcoming Barriers for Nitrate Electrochemical Reduction: By-Passing Water Hardness.

688   *Water Research* **2022**, *225*, 119118. https://doi.org/10.1016/j.watres.2022.119118.

689   (15) Chen, F.-Y.; Wu, Z.-Y.; Gupta, S.; Rivera, D. J.; Lambeets, S. V.; Pecaut, S.; Kim, J. Y. T.; Zhu, P.;

690   Finfrock, Y. Z.; Meira, D. M.; King, G.; Gao, G.; Xu, W.; Cullen, D. A.; Zhou, H.; Han, Y.; Perea, D.

691   E.; Muhich, C. L.; Wang, H. Efficient Conversion of Low-Concentration Nitrate Sources into

692   Ammonia on a Ru-Dispersed Cu Nanowire Electrocatalyst. *Nat. Nanotechnol.* **2022**, *17* (7), 759–767.

693   https://doi.org/10.1038/s41565-022-01121-4.

694   (16) Li, J.; Zhan, G.; Yang, J.; Quan, F.; Mao, C.; Liu, Y.; Wang, B.; Lei, F.; Li, L.; Chan, A. W. M.; Xu,

695   L.; Shi, Y.; Du, Y.; Hao, W.; Wong, P. K.; Wang, J.; Dou, S.-X.; Zhang, L.; Yu, J. C. Efficient

696   Ammonia Electrosynthesis from Nitrate on Strained Ruthenium Nanoclusters. *J. Am. Chem. Soc.* **2020**,

697   *142* (15), 7036–7046. https://doi.org/10.1021/jacs.0c00418.

698   (17) Lim, J.; Liu, C.-Y.; Park, J.; Liu, Y.-H.; Senftle, T. P.; Lee, S. W.; Hatzell, M. C. Structure Sensitivity

699   of Pd Facets for Enhanced Electrochemical Nitrate Reduction to Ammonia. *ACS Catal.* **2021**, *11* (12),

700   7568–7577. https://doi.org/10.1021/acscatal.1c01413.

701   (18) Li, P.; Jin, Z.; Fang, Z.; Yu, G. A Single-Site Iron Catalyst with Preoccupied Active Centers That

702   Achieves Selective Ammonia Electrosynthesis from Nitrate. *Energy Environ. Sci.* **2021**, *14* (6), 3522–

703   3531. https://doi.org/10.1039/D1EE00545F.

704   (19) Wu, Z.-Y.; Karamad, M.; Yong, X.; Huang, Q.; Cullen, D. A.; Zhu, P.; Xia, C.; Xiao, Q.; Shakouri,

705   M.; Chen, F.-Y.; Kim, J. Y. (Timothy); Xia, Y.; Heck, K.; Hu, Y.; Wong, M. S.; Li, Q.; Gates, I.;

706   Siahrostami, S.; Wang, H. Electrochemical Ammonia Synthesis via Nitrate Reduction on Fe Single

707   Atom Catalyst. *Nat Commun* **2021**, *12* (1), 2870. https://doi.org/10.1038/s41467-021-23115-x.

708   (20) Li, J.; Li, M.; An, N.; Zhang, S.; Song, Q.; Yang, Y.; Liu, X. Atomically Dispersed Fe Atoms Anchored

709   on S and N–Codoped Carbon for Efficient Electrochemical Denitrification. *Proceedings of the*

710   *National Academy of Sciences* **2021**, *118* (33), e2105628118. https://doi.org/10.1073/pnas.2105628118.

711   (21) Jia, R.; Wang, Y.; Wang, C.; Ling, Y.; Yu, Y.; Zhang, B. Boosting Selective Nitrate Electroreduction

712   to Ammonium by Constructing Oxygen Vacancies in TiO2. *ACS Catal.* **2020**, *10* (6), 3533–3540.

713   https://doi.org/10.1021/acscatal.9b05260.

714   (22) Wang, Y.; Zhou, W.; Jia, R.; Yu, Y.; Zhang, B. Unveiling the Activity Origin of a Copper-Based

715   Electrocatalyst for Selective Nitrate Reduction to Ammonia. *Angewandte Chemie International Edition*

716   **2020**, *59* (13), 5350–5354. https://doi.org/10.1002/anie.201915992.

717   (23) McEnaney, J. M.; Blair, S. J.; Nielander, A. C.; Schwalbe, J. A.; Koshy, D. M.; Cargnello, M.; Jaramillo,

718   T. F. Electrolyte Engineering for Efficient Electrochemical Nitrate Reduction to Ammonia on a

719   Titanium   Electrode.   *ACS   Sustainable   Chem.   Eng.*   **2020**,   *8*   (7),   2672–2681.

720   https://doi.org/10.1021/acssuschemeng.9b05983.

721   (24) Wang, Y.; Xu, A.; Wang, Z.; Huang, L.; Li, J.; Li, F.; Wicks, J.; Luo, M.; Nam, D.-H.; Tan, C.-S.;

722   Ding, Y.; Wu, J.; Lum, Y.; Dinh, C.-T.; Sinton, D.; Zheng, G.; Sargent, E. H. Enhanced Nitrate-to-

51

Ammonia Activity on Copper–Nickel Alloys via Tuning of Intermediate Adsorption. *J. Am. Chem. Soc.* **2020**, *142* (12), 5702–5708. https://doi.org/10.1021/jacs.9b13347.

(25) Chen, G.-F.; Yuan, Y.; Jiang, H.; Ren, S.-Y.; Ding, L.-X.; Ma, L.; Wu, T.; Lu, J.; Wang, H. Electrochemical Reduction of Nitrate to Ammonia via Direct Eight-Electron Transfer Using a Copper–Molecular Solid Catalyst. *Nat Energy* **2020**, *5* (8), 605–613. https://doi.org/10.1038/s41560-020-0654-1.

(26) Chen, J. G.; Crooks, R. M.; Seefeldt, L. C.; Bren, K. L.; Bullock, R. M.; Darensbourg, M. Y.; Holland, P. L.; Hoffman, B.; Janik, M. J.; Jones, A. K.; Kanatzidis, M. G.; King, P.; Lancaster, K. M.; Lymar, S. V.; Pfromm, P.; Schneider, W. F.; Schrock, R. R. Beyond Fossil Fuel–Driven Nitrogen Transformations. *Science* **2018**, *360* (6391). https://doi.org/10.1126/science.aar6611.

(27) Xu, S.; Ashley, D. C.; Kwon, H.-Y.; Ware, G. R.; Chen, C.-H.; Losovyj, Y.; Gao, X.; Jakubikova, E.; Smith, J. M. A Flexible, Redox-Active Macrocycle Enables the Electrocatalytic Reduction of Nitrate to Ammonia by a Cobalt Complex. *Chem. Sci.* **2018**, *9* (22), 4950–4958. https://doi.org/10.1039/C8SC00721G.

(28) Jackels, S. C.; Farmery, Keith.; Barefield, E. Kent.; Rose, N. J.; Busch, D. H. Tetragonal Cobalt(III) Complexes Containing Tetradentate Macrocyclic Amine Ligands with Different Degrees of Unsaturation. *Inorg. Chem.* **1972**, *11* (12), 2893–2901. https://doi.org/10.1021/ic50118a008.

(29) Cole-Hamilton, D. J. Homogeneous Catalysis--New Approaches to Catalyst Separation, Recovery, and Recycling. *Science* **2003**, *299* (5613), 1702–1706. https://doi.org/10.1126/science.1081881.

(30) Hu, K.; Zhou, P.; Yang, Y.; Hall, T.; Nie, G.; Yao, Y.; Duan, X.; Wang, S. Degradation of Microplastics by a Thermal Fenton Reaction. *ACS EST Eng.* **2022**, *2* (1), 110–120. https://doi.org/10.1021/acsestengg.1c00323.

(31) Sun, J.; Jennepalli, S.; Lee, M.; Jones, A.; O'Carroll, D. M.; Manefield, M. J.; Bhadbhade, M.; Åkermark, B.; Das, B.; Kumar, N. Efficient Reductive Defluorination of Branched PFOS by Metal–Porphyrin Complexes. *Environ. Sci. Technol.* **2022**, *56* (12), 7830–7839. https://doi.org/10.1021/acs.est.1c08254.

(32) Niemann, V. A.; Benedek, P.; Guo, J.; Xu, Y.; Blair, S. J.; Corson, E. R.; Nielander, A. C.; Jaramillo, T. F.; Tarpeh, W. A. Co-Designing Electrocatalytic Systems with Separations To Improve the Sustainability of Reactive Nitrogen Management. *ACS Catal.* **2023**, *13* (9), 6268–6279. https://doi.org/10.1021/acscatal.3c00933.

(33) Niemann, V. A.; Benedek, P.; Guo, J.; Xu, Y.; Blair, S. J.; Corson, E. R.; Nielander, A. C.; Jaramillo, T. F.; Tarpeh, W. A. Co-Designing Electrocatalytic Systems with Separations To Improve the Sustainability of Reactive Nitrogen Management. *ACS Catal.* **2023**, *13* (9), 6268–6279. https://doi.org/10.1021/acscatal.3c00933.

(34) Gao, J.; Shi, N.; Li, Y.; Jiang, B.; Marhaba, T.; Zhang, W. Electrocatalytic Upcycling of Nitrate Wastewater into an Ammonia Fertilizer via an Electrified Membrane. *Environ. Sci. Technol.* **2022**, *56* (16), 11602–11613. https://doi.org/10.1021/acs.est.1c08442.

(35) Gao, J.; Shi, N.; Guo, X.; Li, Y.; Bi, X.; Qi, Y.; Guan, J.; Jiang, B. Electrochemically Selective Ammonia Extraction from Nitrate by Coupling Electron- and Phase-Transfer Reactions at a Three-Phase Interface. *Environ. Sci. Technol.* **2021**, *55* (15), 10684–10694. https://doi.org/10.1021/acs.est.0c08552.

(36) Zheng, W.; Zhu, L.; Yan, Z.; Lin, Z.; Lei, Z.; Zhang, Y.; Xu, H.; Dang, Z.; Wei, C.; Feng, C. Self-Activated Ni Cathode for Electrocatalytic Nitrate Reduction to Ammonia: From Fundamentals to Scale-Up for Treatment of Industrial Wastewater. *Environ. Sci. Technol.* **2021**, *55* (19), 13231–13243. https://doi.org/10.1021/acs.est.1c02278.

(37) Kim, K.; Zagalskaya, A.; Ng, J. L.; Hong, J.; Alexandrov, V.; Pham, T. A.; Su, X. Coupling Nitrate Capture with Ammonia Production through Bifunctional Redox-Electrodes. *Nat Commun* **2023**, *14* (1), 823. https://doi.org/10.1038/s41467-023-36318-1.

(38) Liu, M. J.; Miller, D. M.; Tarpeh, W. A. Reactive Separation of Ammonia from Wastewater Nitrate via Molecular Electrocatalysis. *Environ. Sci. Technol. Lett.* **2023**, *10* (5), 458–463. https://doi.org/10.1021/acs.estlett.3c00205.

774   (39) Savéant, J. M.; Costentin, C. *Elements of Molecular and Biomolecular Electrochemistry: An*

775   *Electrochemical Approach to Electron Transfer Chemistry*, Second edition.; Wiley: Hoboken, NJ,

776   2019.

777   (40) Guo, J.; Brimley, P.; Liu, M. J.; Corson, E. R.; Muñoz, C.; Smith, W. A.; Tarpeh, W. A. Mass Transport

778   Modifies the Interfacial Electrolyte to Influence Electrochemical Nitrate Reduction. *ACS Sustainable*

779   *Chem. Eng.* **2023**. https://doi.org/10.1021/acssuschemeng.3c01057.

780   (41) Bhugun, I.; Lexa, D.; Savéant, J.-M. Catalysis of the Electrochemical Reduction of Carbon Dioxide by

781   Iron(0) Porphyrins. Synergistic Effect of Lewis Acid Cations. *J. Phys. Chem.* **1996**, *100* (51), 19981–

782   19985. https://doi.org/10.1021/jp9618486.

783   (42) Pérez-González, A.; Urtiaga, A. M.; Ibáñez, R.; Ortiz, I. State of the Art and Review on the Treatment

784   Technologies of Water Reverse Osmosis Concentrates. *Water Research* **2012**, *46* (2), 267–283.

785   https://doi.org/10.1016/j.watres.2011.10.046.

786   (43) Mohammadi, R.; Ramasamy, D. L.; Sillanpää, M. Enhancement of Nitrate Removal and Recovery

787   from Municipal Wastewater through Single- and Multi-Batch Electrodialysis: Process Optimisation

788   and   Energy   Consumption.   *Desalination*   **2021**,   *498*,   114726.

789   https://doi.org/10.1016/j.desal.2020.114726.

790   (44) Hawks, S. A.; Cerón, M. R.; Oyarzun, D. I.; Pham, T. A.; Zhan, C.; Loeb, C. K.; Mew, D.; Deinhart,

791   A.; Wood, B. C.; Santiago, J. G.; Stadermann, M.; Campbell, P. G. Using Ultramicroporous Carbon

792   for the Selective Removal of Nitrate with Capacitive Deionization. *Environ. Sci. Technol.* **2019**, *53*

793   (18), 10863–10870. https://doi.org/10.1021/acs.est.9b01374.

794   (45) Chen, H.; Rose, M.; Fleming, M.; Souizi, S.; Shashvatt, U.; Blaney, L. Recent Advances in Donnan

795   Dialysis Processes for Water/Wastewater Treatment and Resource Recovery: A Critical Review.

796   *Chemical Engineering Journal* **2023**, *455*, 140522. https://doi.org/10.1016/j.cej.2022.140522.

797   (46) Pennino, M. J.; Leibowitz, S. G.; Compton, J. E.; Hill, R. A.; Sabo, R. D. Patterns and Predictions of

798   Drinking Water Nitrate Violations across the Conterminous United States. *Science of The Total*

799   *Environment* **2020**, *722*, 137661. https://doi.org/10.1016/j.scitotenv.2020.137661.

800   (47) Janssen, M.; Müller, C.; Vogt, D. Recent Advances in the Recycling of Homogeneous Catalysts Using

801   Membrane Separation. *Green Chem.* **2011**, *13* (9), 2247–2257. https://doi.org/10.1039/C1GC15264E.

802   (48) Kogler, A.; Farmer, M.; Simon, J. A.; Tilmans, S.; Wells, G. F.; Tarpeh, W. A. Systematic Evaluation

803   of Emerging Wastewater Nutrient Removal and Recovery Technologies to Inform Practice and

804   Advance Resource Efficiency. *ACS EST Eng.* **2021**, *1* (4), 662–684.

805   https://doi.org/10.1021/acsestengg.0c00253.

806   (49) Gayen, P.; Spataro, J.; Avasarala, S.; Ali, A.-M.; Cerrato, J. M.; Chaplin, B. P. Electrocatalytic

807   Reduction of Nitrate Using Magnéli Phase TiO2 Reactive Electrochemical Membranes Doped with

808   Pd-Based Catalysts. *Environ. Sci. Technol.* **2018**, *52* (16), 9370–9379.

809   https://doi.org/10.1021/acs.est.8b03038.

810   (50) Wang, J.; Wang, S.; Zhang, Z.; Wang, C. Preparation of Cu/GO/Ti Electrode by Electrodeposition and

811   Its Enhanced Electrochemical Reduction for Aqueous Nitrate. *Journal of Environmental Management*

812   **2020**, *276*, 111357. https://doi.org/10.1016/j.jenvman.2020.111357.

813   (51) Cheng, H.; Scott, K.; Christensen, P. A. Paired Electrolysis in a Solid Polymer Electrolyte Reactor—

814   Simultaneously Reduction of Nitrate and Oxidation of Ammonia. *Chemical Engineering Journal* **2005**,

815   *108* (3), 257–268. https://doi.org/10.1016/j.cej.2005.02.028.

816   (52) Katsounaros, I.; Dortsiou, M.; Kyriacou, G. Electrochemical Reduction of Nitrate and Nitrite in

817   Simulated Liquid Nuclear Wastes. *Journal of Hazardous Materials* **2009**, *171* (1), 323–327.

818   https://doi.org/10.1016/j.jhazmat.2009.06.005.

819   (53) Kogler, A.; Farmer, M.; Simon, J. A.; Tilmans, S.; Wells, G. F.; Tarpeh, W. A. Systematic Evaluation

820   of Emerging Wastewater Nutrient Removal and Recovery Technologies to Inform Practice and

821   Advance Resource Efficiency. *ACS EST Eng.* **2021**, *1* (4), 662–684.

822   https://doi.org/10.1021/acsestengg.0c00253.

823   (54) Soloveichik, G. Electrochemical Synthesis of Ammonia as a Potential Alternative to the Haber–Bosch

824   Process. *Nat Catal* **2019**, *2* (5), 377–380. https://doi.org/10.1038/s41929-019-0280-0.

825   (55) Wu, D.; Li, X.; Li, X. Toward Energy Neutrality in Municipal Wastewater Treatment: A Systematic

826   Analysis of Energy Flow Balance for Different Scenarios. *ACS EST Water* **2021**, *1* (4), 796–807.

827   https://doi.org/10.1021/acsestwater.0c00154.

828   (56) Ams_3657.Pdf. https://www.ams.usda.gov/mnreports/ams_3657.pdf (accessed 2023-10-18).

829   (57) Estimation of U.S. Sewer Residence Time Distributions for National-Scale Risk Assessment of down-

830   the-Drain Chemicals. *Science of The Total Environment* **2017**, *603–604*, 445–452.

831   https://doi.org/10.1016/j.scitotenv.2017.06.075.

832   (58) Cole, W. J.; Frew, B. A.; Gagnon, P. J.; Richards, J.; Sun, Y.; Margolis, R. M.; Woodhouse, M. A.

833   *SunShot 2030 for Photovoltaics (PV): Envisioning a Low-Cost PV Future*; NREL/TP--6A20-68105,

834   1392206; 2017; p NREL/TP--6A20-68105, 1392206. https://doi.org/10.2172/1392206.

835   (59) Lazouski, N.; Limaye, A.; Bose, A.; Gala, M. L.; Manthiram, K.; Mallapragada, D. S. Cost and

836   Performance Targets for Fully Electrochemical Ammonia Production under Flexible Operation. *ACS*

837   *Energy Lett.* **2022**, *7* (8), 2627–2633. https://doi.org/10.1021/acsenergylett.2c01197.

838   (60) Fernandez, C. A.; Hatzell, M. C. Editors' Choice—Economic Considerations for Low-Temperature

839   Electrochemical Ammonia Production: Achieving Haber-Bosch Parity. *J. Electrochem. Soc.* **2020**, *167*

840   (14), 143504. https://doi.org/10.1149/1945-7111/abc35b.

841   (61) Niemann, V. A.; Benedek, P.; Guo, J.; Xu, Y.; Blair, S. J.; Corson, E. R.; Nielander, A. C.; Jaramillo,

842   T. F.; Tarpeh, W. A. Co-Designing Electrocatalytic Systems with Separations To Improve the

843   Sustainability of Reactive Nitrogen Management. *ACS Catal.* **2023**, 6268–6279.

844   https://doi.org/10.1021/acscatal.3c00933.

845   (62) Miller, D.; Abels, K.; Guo, J.; Williams, K.; Liu, M.; Tarpeh, W. Electrochemical Wastewater Refining:

846   A Vision for Circular Chemical Manufacturing. ChemRxiv April 5, 2023.

847   https://doi.org/10.26434/chemrxiv-2023-1tdxx.

848   (63) Chen, Y.; Ammari-Azar, P.; Liu, H.; Lee, J.; Xi, Y.; Castellano, M. J.; Gu, S.; Li, W. Sustainable

849   Waste-Nitrogen Upcycling Enabled by Low-Concentration Nitrate Electrodialysis and High-

850   Performance Ammonia Electrosynthesis. *EES. Catal.* **2023**, *1* (4), 504–515.

851   https://doi.org/10.1039/D3EY00058C.

852   (64) Marin, D. H.; Perryman, J. T.; Hubert, M. A.; Lindquist, G. A.; Chen, L.; Aleman, A. M.; Kamat, G.

853   A.; Niemann, V. A.; Stevens, M. B.; Regmi, Y. N.; Boettcher, S. W.; Nielander, A. C.; Jaramillo, T. F.

854   Hydrogen Production with Seawater-Resilient Bipolar Membrane Electrolyzers. *Joule* **2023**, *7* (4),

855   765–781. https://doi.org/10.1016/j.joule.2023.03.005.

856

857

858